Investigations of novel properties of 2D and other inorganic nanostructures

A Thesis submitted in partial fulfilment for the degree of

Master of Science

as a part of

Integrated Ph.D. Programme (Chemical Science)

by

Manaswee Barua

New Chemistry Unit

Jawaharlal Nehru Centre for Advanced Scientific Research

(A Deemed University)

Jakkur, Bangalore-560064

India

March 2018

Dedicated to my family and teachers

DECLARATION

I hereby declare that the matter embodied in the thesis entitled "**Investigations of novel properties of 2D and other inorganic nanostructures**" is the result of investigations carried out by me at the New Chemistry Unit, Jawaharlal Nehru Centre for Advanced Scientific Research, Bengaluru, India under the supervision of Prof. C. N. R. Rao and that it has not been submitted elsewhere for the award of any degree or diploma.

In keeping with the general practice in reporting scientific investigations, due acknowledgement has been made wherever the work described is based on findings of other investigators. Any omission that might have occurred by oversight or error of judgement is regretted.

Date: ----------

Bengaluru, India Manaswee Barua

CERTIFICATE

I hereby declare that the matter embodied in the thesis entitled "**Investigations of novel properties of 2D and other inorganic nanostructures**" has been carried out by Ms. Manaswee Barua at the New Chemistry Unit, Jawaharlal Nehru Centre for Advanced Scientific Research, Bengaluru, India under my supervision and that it has not been submitted elsewhere for the award of any degree or diploma.

Date:

Bengaluru, India

Prof. C. N. R. Rao

ACKNOWLEDGEMENTS

First and foremost, I take this opportunity to express my deepest gratitude to my research supervisor, Prof. C. N. R. Rao, FRS, for introducing me to the fascinating fields of 'nanomaterials'. It was his enthusiasm that instigated in me the desire to pursue science and has continued to inspire me ever since. His innovative ideas and ability to handle any problem in the simplest of the ways has been the strength behind the completion of this work. It has been a fulfilling experience to work under his encouraging and full spirited guidance. He has not only been instrumental in shaping up my research, my career but my entire personality, my outlook towards life as a whole.

My sincere thanks to my collaborators, Prof. Swapan K. Pati, Prof. U. Ramamurty, Ms. Arkamita Bandyopadhyay, Mr. Abhishek Chaturvedi and Ms. Madhulika Mazumdar for their valuable contributions and discussions.

My work would have been incomplete without the help of my co-workers – Mr. Sreedhara, Dr. Pramoda, Dr. Vishnoi, Mr. Rajesh, Mr. S. Manjunath and Ms. Fatahi, who worked with me in different projects. Special thanks to them all. I shall remain ever thankful to all my seniors for their valuable suggestions. It has been a wonderful experience working with all my past and present labmates Dr. R. Saha, Dr. Gopal, Dr. R. Kumar, Dr. S. Dey, Dr. P. Vishnoi, Dr. D. Narang, Dr. Manjunath, Dr. M. Jaiswal, Dr. Pramoda, Dr. Jana, Mr. Sreedhara, Mr. Uttam, Mr. Roy, Mr. Chhetri, Mr. Monis, Mr. S. Manjunatha, Mr. Rajesh Mr. Amit, Mr. Navin, Mr. Rohit, Dr. Kaur, Mr. Reetendra and Mr. Swaraj and I thank them all for their help in various occasions.

I thank the faculties namely Prof. H. Ila, Prof. S**.** Balasubramanian**,** Prof. A. Sundaresan, Prof. Eswaramoorthy, Prof. Sridhar Rajaram, Prof. Shobhana Narasimhan, Prof. T. K. Maji, Prof.

S. J. George, Prof. R. Viswanatha, Prof. Jayanta Haldar, Prof. Kanishka Biswas, Dr. Meher Prakash, Prof. Sebastian C. Peter and Dr. Agasti for all the illuminating courses and discussions.

I thank the timely help of the technical staff namely Ms. N. R. Selvi, Mrs. T. Usha, Mr. Vasu, Mr. Anil, Mr. Srinath, Mr. Mahesh, Dr. Joy, Mr. Kannan, Mr. Jagadish and Mr. Shivkumar. I thank Mrs. Shashi, Mrs. Sudha, Mr. Gowda and Mr. Victor for their help in various aspects.

I thank JNCASR and DST for research fellowship.

I extend my sincere thanks to hostel, Admin, Academic, Library, Dining hall and Dhanvantari and other departmental staff for all their help.

I take this opportunity to thank Mrs. Indumati Rao for all the affection and love I have received from her. Her enthusiasm age notwithstanding has been a source of inspiration for me. I consider myself blessed to have received all these care and more than everything the wise words of advice every now and then. I take this opportunity to thank Mr. Sanjay Rao for his hospitality.

Thanks to all my friends and batchmates with whom I started my life at this centre and whose cheerful company made these three years of life so cherishable.

Finally, I thank my parents and family members and Almightly for everything.

PREFACE

This thesis contains results of investigations carried out on the surface chemistry of 2D materials such as graphene, BN and borocarbonitrides (BCN), mechanical properties of BCN incorporated polymer composites and donor-acceptor interactions of 2D phosphorene and chalcogenide nanoparticles. A brief report on the results of preliminary investigations of germanane is also included.

It contains the following chapters:

Chapter 1: Quantification of surface functionalities on graphene, boron nitride and borocarbonitrides by fluorescence labeling

Chapter 2: Mechanical and thermal properties of borocarbonitrides nanosheet-reinforced polymer nanocomposites

Chapter 3: Charge-transfer interactions of 2D phosphorene and phosphorene quantum dots

Chapter 4: Covalent functionalization of nanoparticles of semiconducting metal chalcogenides

Chapter 5: Pure germanane

TABLE OF CONTENTS

CHAPTER 1

Quantification of surface functionalities on graphene, boron nitride and borocarbonitrides by fluorescence labeling*

SUMMARY

Considering the important role played by surface functionalities on the properties of 2D materials, we have carried out a careful investigation to obtain quantitative estimates of the functionalities on graphene, boron nitride and borocarbonitrides, by employing fluorescence labeling. Supercapacitor performance and oxygen reduction reactivity of the borocarbonitrides have been measured along with their surface areas to illustrate the importance of surface functionalities.

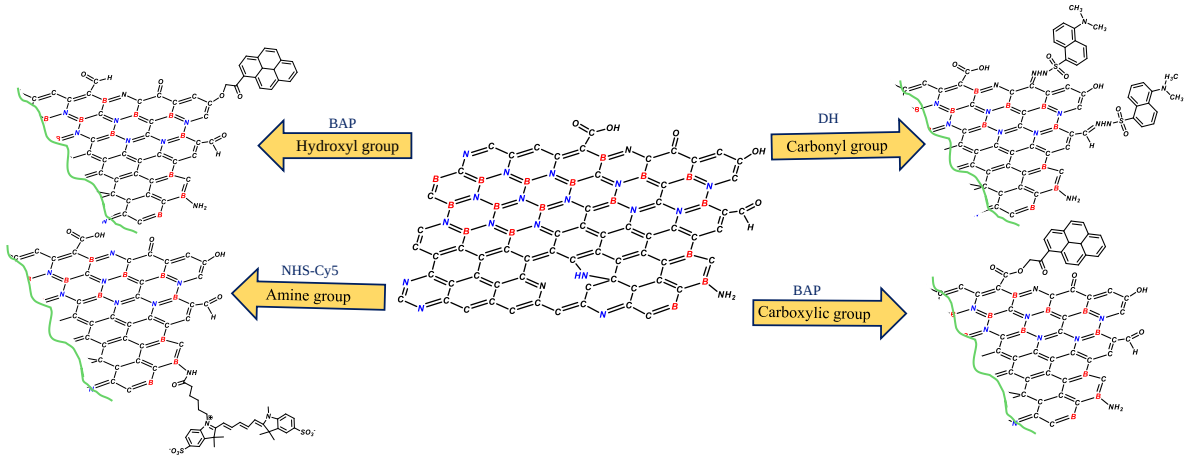

**A paper related to this work has appeared in Chemical Physics Letters (2017)*

1.1 Introduction

Characterization of material surfaces is of great importance in understanding the reactivity and properties of materials. In many recent studies, surface characterization of materials is generally limited to reporting the surface area and qualitative identification of the functional groups present on the surface, the latter being enabled by X-ray photoelectron spectroscopy (XPS) or Fourier-transform infrared spectroscopy (FTIR). It is however desirable to have a quantitative estimation of the surface functional groups. This is relevant since the presence of functional groups indeed affects the properties of the materials when used in various applications. A typical example would be the use of carbon materials in supercapacitors and energy devices. Graphene and related two-dimensional materials present a variety of oxygen containing functional groups on their surfaces. Boron nitride is another layered two-dimensional material with amine groups on its surface. Borocarbonitrides (BCN) are a class of layered two-dimensional materials having both graphene-like domains and BN-like domains along with some B-C-N domains. Surfaces of BCN can contain surface functional groups common to both graphene and BN. What makes BCN a very interesting material is that it is a highly heterogeneous material where the number of surface functional groups and the corresponding surface areas can be varied by varying the composition. In our present study, we have quantitatively characterised the surfaces of graphene, BN and BCN by employing fluorescence spectroscopy[1]. This is done by chemically labeling the surface functional groups by fluorescent probes, wherein fluorescence labeling of surface species (FLOSS), helps to detect and quantify the surface functional groups as low as10^9 groups/cm^2 [1]. This technique has been used successfully to quantify surface functionalities in carbon nanotubes[2, 3], carbon nanofibers[4, 5], polymer surfaces[6, 7] and epoxy groups[8, 9]. The detection limit of FLOSS is much lower than that of XPS, ToF-SIMS, FTIR and other spectroscopic

techniques[9,10]. In order to show possible relations between surface functionalities and specific properties with potential applications, we have measured supercapacitor characteristics as well as oxygen reduction reaction activity of borocarbonitrides of different compositions[11,12].

1.2 Experimental

Materials

All the chemicals used were of high purity and were used without further purification. Natural graphite (Alfa Aesar, 99.9995%), sulphuric acid (SDFCL, 98%), potassium permanganate (Merck), sodium nitrate (SDFCL), hydrogen peroxide (Merck), boric acid (Merck), urea (SDFCL), water (Millipore).

Synthesis

Synthesis of graphene oxide (GO) and exfoliated graphene (EG)

Graphene oxide was synthesized by the modified Hummer's method[13,14]. In a typical synthesis, 150 mL of concentrated sulphuric acid was slowly added to a 1L beaker, containing 3 g each of natural graphite flakes and sodium nitrate, kept in an ice bath. The mixture was stirred for 15 minutes and then 20 g of potassium permanganate was added into it, while the beaker is still in ice bath. The beaker was then transferred to an oil bath maintained at 40 °C and stirred for an hour. To the resulting dark brown suspension, 150 mL of water was added and the suspension was further stirred at 75 °C for 10 minutes. Finally, 30 mL of H_2O_2 in 300 mL water was added to the reaction mixture. The brown coloured suspension obtained was washed several times with water until the pH of the solution became neutral. The suspension was then lyophilised to obtain flaky brown coloured solid GO. EG was obtained by thermal exfoliation of GO at 1050 °C under N_2 atmosphere.

Synthesis of Borocarbonitrides (BCN) and boron nitride (BN)

EG, boric acid and urea were dispersed in 20 mL water and then stirred at 70 °C to obtain slurry. This slurry was then transferred into an alumina boat and the reaction mixture was heated to 900 °C under N_2 atmosphere for 5 hours to get borocarbonitrides[12]. By varying the boric acid to carbon ratio, four different compositions of BCN were obtained (**Table** 1). BN was synthesized in a similar way by using boric acid and urea only[15].

Characterization

Powder X-ray diffraction patterns were collected using a Bruker D8 Discover diffractometer using Cu-Kα radiation. Raman spectra were collected in the backscattering geometry using a 632 nm HeNe laser with a Jobin Yvon LabRam HR 800 spectrometer. Fourier transform infrared spectra (FTIR) were recorded in a Bruker FTIR specrometer in KBr mode. Gravimetric compositions BCN samples were determined by thermogravimetric analyses carried out in an oxygen atmosphere with a Metler Toledo TGA-850 TG analyser at the rate of 3 °C/min. Elemental mapping of B, N and C were carried out using energy dispersive X-ray spectroscopy (EDX) and morphology was obtained using scanning electron microscopy Nova NanoSEM 600 FESEM. Chemical compositions and bonding nature of the samples were determined by X-ray photoelectron (XP) spectroscopy in an Omicron nanotechnology spectrometer, using monochromatic Mg-K_α as X-ray source. Atomic force microscope (AFM) images were obtained on SiO_2/Si substrates in tapping mode using Bruker Innova instrument. Transmission electron microscopy (TEM) images were recorded with a FEI Tecnai G^2 S-Twin operated microscope fitted with a Gatan CCD camera. High resolution TEM images, electron energy loss spectra (EELS) and elemental mapping were recorded using Titan (cube) FEI transmission electron microscope with an accelerating voltage 300

kV. N_2 sorption profiles were recorded using a Quantachrome Quandasord-*SI* analyzer. Photoluminescence spectra were recorded with a Fluorolog-3 spectrophotometer fitted with Horiba Jobin Yvon Xe lamp light source. Electrochemical measurements were carried out in a CH instrument

Quantification of surface groups using fluorescent probes

We have used fluorescence labeling for systematically quantifying the number of surface groups on EG, BN and BCN. The fluorescent probes were chemically attached to specific surface functional groups of these materials as described in literature[3]. In the case of graphene we have used 5-(Dimethylamino)-1-naphthalenesulfonic hydrazide **(**Dansyl hydrazine, DH) for carbonyl group estimation and 1-(bromoacetyl)pyrene (PB) for both carboxylic acid and hydroxyl group detection but under different reaction conditions. For BN, fluorescent probe used for amine group detection was NHS-Cy5 while for hydroxyl group again 1-(bromoacetyl)pyrene was used. In BCN where domains of both BN and graphene would be present along with some B-C-N domains, we expect the material to have all the above mentioned functional groups and the chemical estimation were carried out in a similar way.

For estimation of surface functional groups, calibration curves of the different dyes were obtained over a known concentration range. The concentrations of the functional groups were determined by measuring the fluorescence intensity of the particular dye solution before contact with the sample and after the fluorescence labeling reaction with the labeled sample removed from the solution. One of the major problems in fluorescent labeling is the possibility of physical adsorption of the dye molecules on the surface without covalently have linking to the surface groups. In order to validate our results and to know physisorption we

carried out series of control experiments.

Fluorescence labeling of carbonyl groups using Dansyl hydrazine (DH)[16]

To a 3 mg of sample under study, a 10 mL 0.68 mM solution of DH in methanol, 1.8 mL of 0.1M hydrochloric acid solution in methanol was added. The resulting solution was stirred in dark at room temperature for 62 hours. After the completion of reaction the resulting solutions were centrifuged and supernatant was collected in a flask. The remaining sample was washed several times with fresh methanol to remove any physisorbed dye molecules. The washings were collected in the same flask and diluted to known volume to record the PL. A control experiment was carried out without the sample under same conditions. Also, physisorption experiments were carried out without the reagent.

Fluorescence labeling of carboxylic acid groups using 1-(bromoacetyl)pyrene (PB)[17]

Chemical tagging of carboxylic acid groups using 1-(bromoacetyl)pyrene has been carried out using standard procedure. To a 2 mg of sample under study, a 2 mL 1.35 mM solution of 1-(bromoacetyl)pyrene in DMF, 0.54 mg of K_2CO_3 and 0.45 mg of KI were added. The resulting solution was stirred in dark at 50 °C for 12 hours. After the completion of reaction the resulting solutions were centrifuged and supernatant was collected in a flask. The remaining sample was washed several times with fresh DMF to remove any physisorbed dye molecules. The washings collected in the same flask and diluted to known volume to record the PL. A control experiment was carried without the sample under same conditions. Also, physisorption experiments were carried out without the reagent.

Fluorescence labeling of hydroxyl groups using 1-(bromoacetyl)pyrene (PB)

To a 2 mg of sample under study, a 2 mL 0.412 mM solution of 1-(bromoacetyl)pyrene in DMF, 0.2 mL of triethylamine (TEA) was added. The resulting solution was stirred in dark at

room temperature for 10 hours. After the completion of reaction the resulting solutions were centrifuged and supernatant was collected in a flask. The remaining sample was washed several times with fresh DMF to remove any physisorbed dye molecules. The washings were collected in the same flask and diluted to known volume to record the PL. A control experiment was carried without the sample under same conditions. Also, physisorption experiments were carried out without the reagent.

Fluorescence labeling of amine groups using N-Hydroxysuccinimide Cy5 (NHS-Cy5)[18]

Fluorescence labeling of amine groups was carried out as described elsewhere. To a 1 mg sample of the material under study, 3 mL of DMSO, a 5µL of 1.382 mM of NHS-Cy5 dye solution and 50 µL of triethylamine (TEA) were added. The resulting solution was stirred in dark at room temperature for 6 hours. After the completion of reaction, the resulting solutions were centrifuged and supernatant was collected in a flask. The remaining sample was washed several times with fresh DMSO to remove any physisorbed dye molecules. The washings were collected in the same flask and diluted to known volume to record the PL. A control experiment was carried without the sample under the same conditions. Physisorption experiments were carried out without the reagent.

Steps involved in the calculation of surface functional groups

Calibration plots for the different fluorescent probes were obtained by plotting PL intensity vs. dye concentration at a particular wavelength. The PL data for all the samples were plotted against the control. The decrease in fluorescent intensity for the samples, at the particular wavelength at which the calibration plot was drawn for the particular probe, was noted. From the calibration plot we obtain the concentration of reacted fluorescent probes. The concentration obtained was multiplied by Avogadro number and divided by the amount of

sample taken to obtain the number of surface functional groups per gram of the material. By dividing this number by the surface area of the material we get the number of groups per unit surface area of the material.

Electrochemical measurements

Supercapacitor performance

Supercapacitor performance was investigated by means of cyclic voltammetry (CV) and galvanostatic charge-discharge measurements in 1 M H2SO4 aqueous electrolyte under three-electrode assembly with a Pt wire as the reference electrode and Ag/AgCl as the counter electrode. The working electrode was a glassy carbon electrode coated with catalyst.

Nafion stock solution was prepared by mixing 50 µL Nafion solution, 4 mL water and 1 mL Propan-2-ol. 4 mg of the material (EG, BN or BCN) was added into 300 uL of Nafion stock solution. This solution was dispersed for 15 minutes and 5 µL of this dispersion was drop-coated on the glassy carbon electrode and allowed to dry in room temperature for 3-4 hours. This was the working electrode.

Cyclic voltammetry measurements were carried out at different scan rates from 5 to 200 mV/s. The specific capacitance (C_{sp}) was calculated using the following formula:

$$\mathrm{Csp} = \frac{2 \times \mathrm{I}}{m \times S}$$

where I is corresponding current from the CV curve at V=0.5 V, m is the amount of sample drop-coated on the electrode and S is the scan rate.

Galvanostatic charge-discharge measurements were carried out at different scan rates from 0.2 to 10 A/g. The specific capacitance (C_{sp}) was calculated using the following formula:

$$\mathrm{Csp} = \frac{2 \times (\frac{\mathrm{I}}{\mathrm{m}})}{dV/dt}$$

where I/m refers to the scan rate and dV/dt is the slope of the discharge plot.

Oxygen reduction reaction (ORR)

ORR catalytic activity of the samples was investigated using a rotating disk electrode (RDE), with a three electrode assembly, in O_2 saturated 0.1 M KOH solution as electrolyte. Pt wire was used as the reference electrode, Ag/AgCl as the counter electrode and a working electrode rotated at different rates from 400 to 2000 rpm, containing the drop coated catalyst. Linear sweep voltammetry measurements of the different samples at 1600 rpm show different ORR onset potentials of the samples.

The number of electron transfer per oxygen molecule for the different catalyst materials was calculated by using the Koutecky-Levich equation:

$$1/I = 1/I_k + 1/I_{lev}$$

where I is the disk current density, I_k is the kinetic current density and I_{lev} is the Levich current density.

$$I^{-1/2} = \omega^{-1/2}/ (0.62 \times n \times F \times A \times C_{O2} \times D_{O2}^{2/3} \times \nu^{-1/6})$$

Where n gives the overall number of electrons transferred, F is the Faraday constant (96485 $Cmol^{-1}$), A is the electrode area (0.0706 cm^2), C_{O2} is the concentration of dissolved oxygen (1.2×10^{-6} $molcm^{-3}$), D_{O2} is the diffusion coefficient of O_2 in 0.1 M KOH (1.9×10^{-5} cm^2s^{-1}) and ν is the kinematic viscosity (0.01).

Number of electron transfer (n) was determined from the slope of $I^{-1/2}$ vs $\omega^{-1/2}$ plot.

1.3 Results and discussion

Material characterization

For our current study, the materials of interest (EG, BN and BCN) were extensively characterized by both spectroscopic and microscopic techniques.

The electron microscopic and atomic force microscopic images of the samples reveal their 2D planar morphology (**Figure**s 1, 2 and 3). The sheets are electron transparent and show wrinkled morphology. We have not observed any differences in nanosheets morphology with

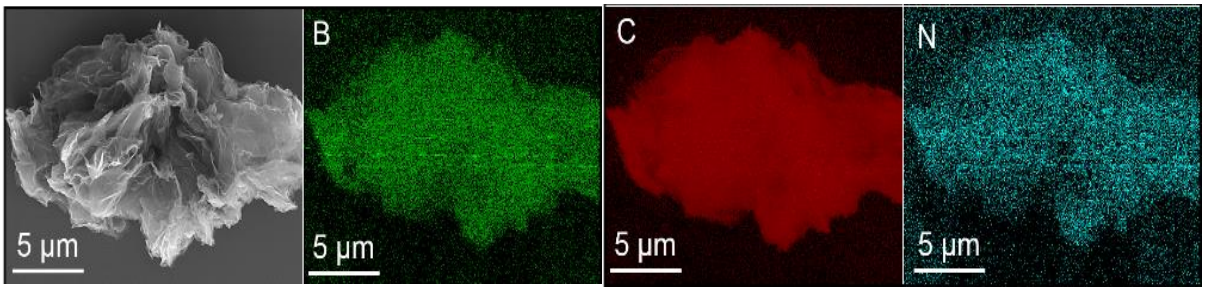

Figure 1: FESEM image of sample along with EDX elemental mapping

changing compositions. Elemental mapping in BCN shows uniform distribution of dopants throughout the sample. The nanosheets display an average height of 3.4 to 3.6 nm irrespective of the composition revealing that the borocarbonitrides comprise 8-10 layers with lateral dimensions of a few µm.

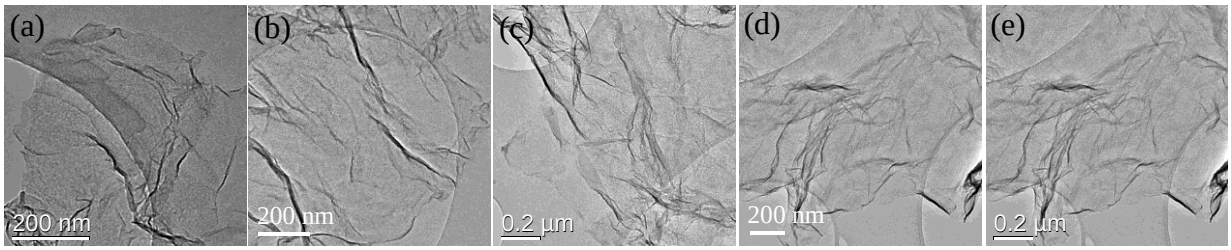

Figure 2: TEM images of (a) EG (b) $(BN)_{0.20}(C)_{0.80}$ (c) $(BN)_{0.50}(C)_{0.50}$ (d) $(BN)_{0.75}(C)_{0.25}$ and (e) $(BN)_{0.90}(C)_{0.10}$

The various BCN compositions were obtained by varying the boric acid to carbon ratio as shown in **Table** 1. The various compositions were determined by TGA. The thermogravimetric curves of BCN in comparison of EG are shown in **Figure** 4. The analysis was carried out by heating the samples upto 800 °C under O_2 atmosphere at 3°C/min. EG shows a sharp loss of about 90% in the temperature range of 300-500 °C, followed by further slow decay. Compared to EG, the various BCN compositions show higher thermal stability.

The gravimetric compositions (as in **Table** 1) of the various BCN samples are calculated from the residual weight at 700 °C compared to EG

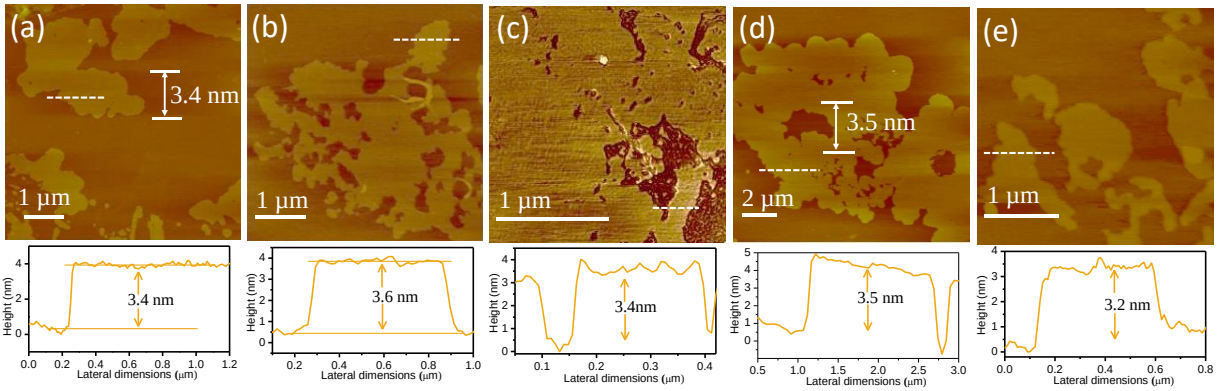

Figure 3: AFM images with corresponding height profile of (a) EG (b) $(BN)_{0.20}(C)_{0.80}$ (c) $(BN)_{0.50}(C)_{0.50}$ (d) $(BN)_{0.75}(C)_{0.25}$ and (e) $(BN)_{0.90}(C)_{0.10}$

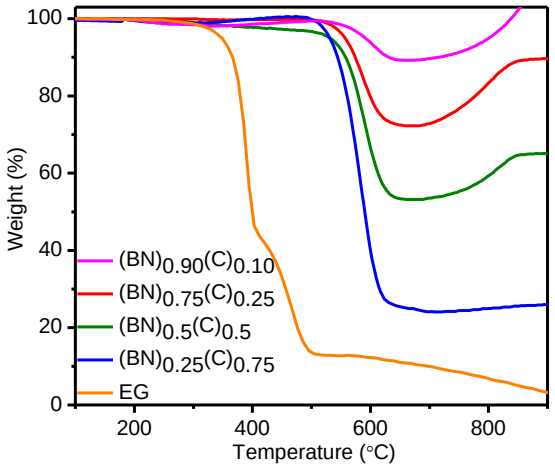

Figure 4: Thermogravimetric plots of different BCN compositions along with EG

Raman spectra of BCN show characteristic bands at 1362 and 1598 cm^{-1} respectively (**Figure** 5). The 1362 cm^{-1} peak dominates with the increase in BN content.

To determine the nature of bonding in BCN, XPS measurements were carried out by drop-casting the well dispersed sample on silicon substrate. Figure 2 shows the XPS spectra of $(BN)_{0.75}(C)_{0.25}$ composition. The B 1s feature of this composition can be deconvoluted into two peaks centred at 191.3 eV and 192.3 eV corresponding to B-C and B-N bonds. High

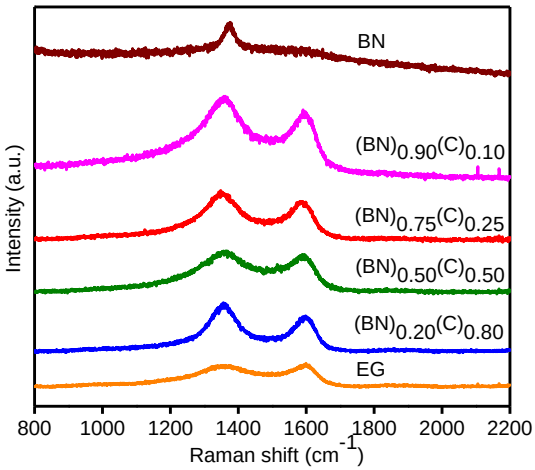

Figure 5: Raman spectra of different BCN compositions along with EG and BN

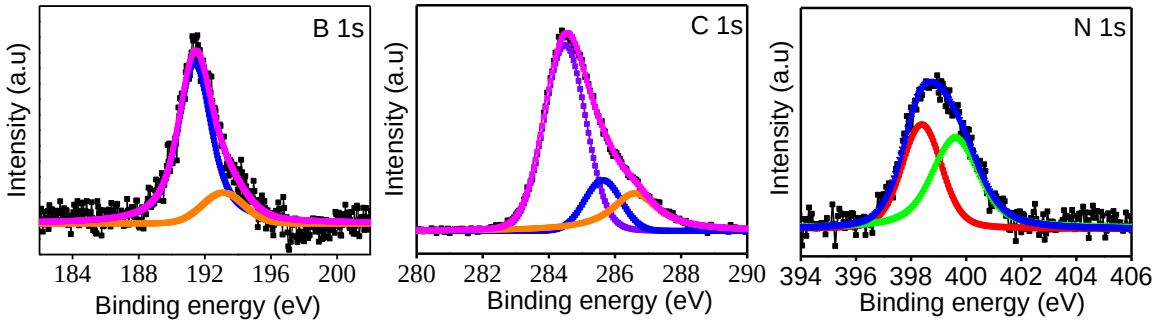

Figure 6: Core-level X-ray photoelectron (XP) spectra of $(BN)_{0.75}(C)_{0.25}$

resolution C 1s spectra can be fitted in to three peaks at 284.4, 285.6 and 286.8 eV due to sp^2 carbons, C-N bonds and surface carbonyls respectively. The N 1s spectrum has a major feature at 398.6 eV due to the pyridinic nitrogen and N-B bonds with another feature at 400.3 eV due to amine content.

The infrared spectrum of BCN shows a characteristic strong band at 1570 cm^{-1} and a weak band around 1728 cm^{-1} due to C=C and carboxyl groups respectively. The broad band around 1100-1250 cm^{-1} is due to C-O stretching and O-H bending vibrations and that around 3200 to 3600 cm^{-1} corresponds to –OH and –NH stretching vibrations.

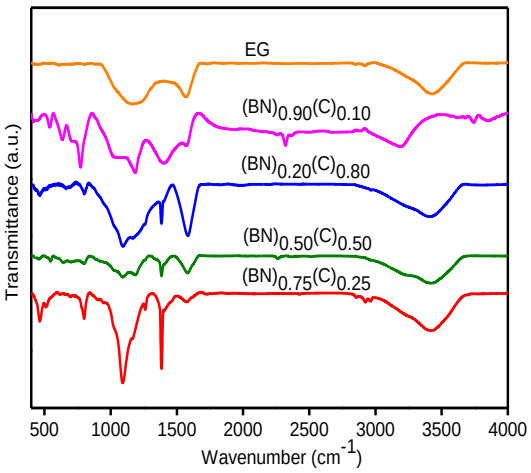

Figure 7: Fourier transform infrared spectrum (FTIR) of EG and various compositions of BCN

Quantification of surface functional groups

Preliminary spectroscopic results revealed the presence of various functional groups on the surfaces of the nanosheets. EG contains O-functionalities as carboxylic acid, carbonyl, hydroxyl and ether on its surface while BN contains amine functionalities apart from surface hydroxyl groups. BCN which contains both C-C domains as in graphene and B-N domains as in BN apart from having B-C-N domains, contains both O- and N- functionalities as in both EG and BN. Quantification of these functional groups is of great significance due to their impact on the properties of materials [19-21]. Commonly used spectroscopic techniques such as FTIR, Raman and XPS [22] as well as titration[23, 24] methods suffer from poor detection limits, and hence cannot be used to quantify the exact amount of functional groups on these materials[5]. We have employed FLOSS for the quantification of the functional groups due to its ability to detect below the detection limit any other available technique till date [16]. **Scheme** 1 gives a pictorial description of chemically labeling the surface groups on EG, BN and BCN by different fluorescent probes.

The carbonyl groups are chemically tagged with the DH probe and the carboxylic and hydroxyl groups with 1-(bromoacetyl) pyrene. In **Figure** 8a, we show the emission spectra of DH of various concentrations with excitation at 350 nm with the corresponding calibration

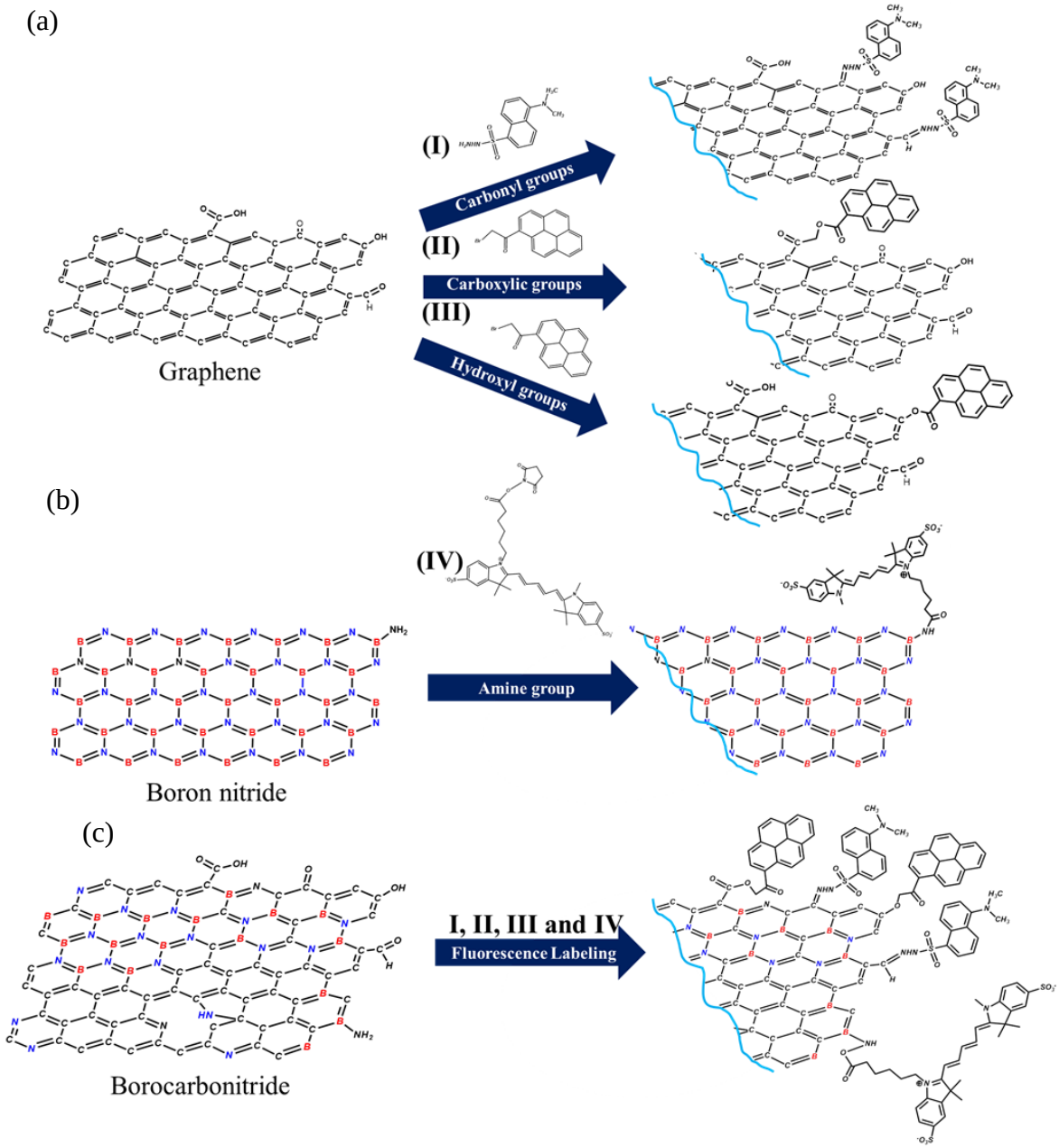

Scheme 1: Schematic representation of surface functional groups on (a) graphene (b) boron nitride and (c) borocarbonitride, and probing them using (I) dansyl hydrazine (carbonyl groups), (II) and (III) 1-(bromoacetyl)pyrene (for carboxylic and hydroxyl groups) and (IV) NHS-Cy5 (for amine groups) fluorescent probes.

curve by monitoring the intensity at 513 nm in the inset. In **Figure** 8b, we illustrate how the reaction of DH with the carbonyl groups on the surface results in the depletion of the fluorescent intensity of the dye due to the covalent attachment of DH molecules to carbonyl groups. The numbers of carbonyl groups present on the surface were estimated using calibration plot. To confirm the quenching of fluorescence intensity due to covalent linking and not due to physisorption, we carried out control experiments without the reagent which showed that there was no observable change in in PL intensity (**Figure** 8c).

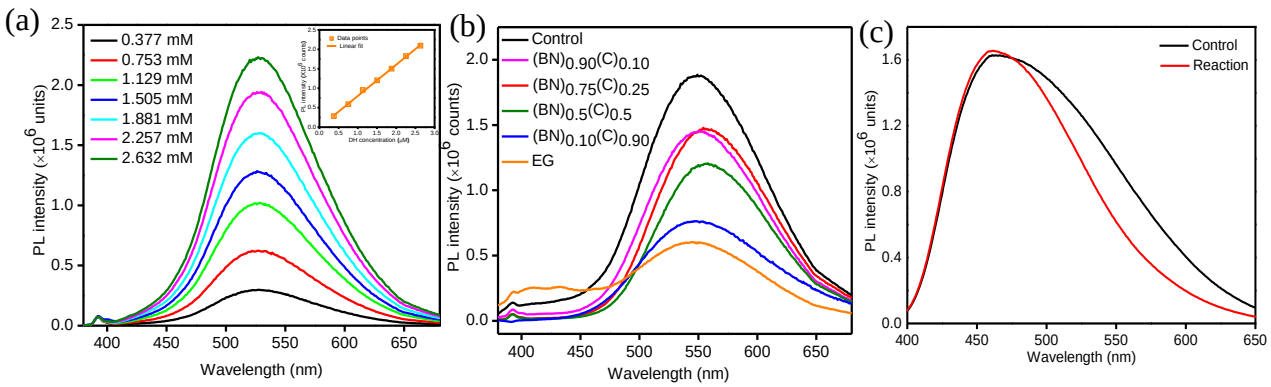

Figure 8: (a) Emission spectra of Dansyl hydrazine (DH) of different concentrations (excitation wavelength 350nm) along with calibration plot at 513 nm (b) Emission spectra of DH reacted with carbonyls of EG and BCN compared with the control experiment (c) Physisorption experiment for DH

Figure 9a shows the PL emission spectra of 1-(bromomoacetyl)pyrene collected over a known range of concentrations with the calibration curve derived by monitoring the intensity at 410 nm displayed in the inset. The PL intensity of carboxylic group reaction shows satisfactory depletion due to the presence of a large number of these groups on the surface (**Figure** 9b). The hydroxyl group reaction shows reasonable decrease in the intensity compared to control reaction (**Figure** 9c). The estimates of carboxylic and hydroxyl groups based on these results are reasonable, although there could be a slight overestimation due to possible side reactions.

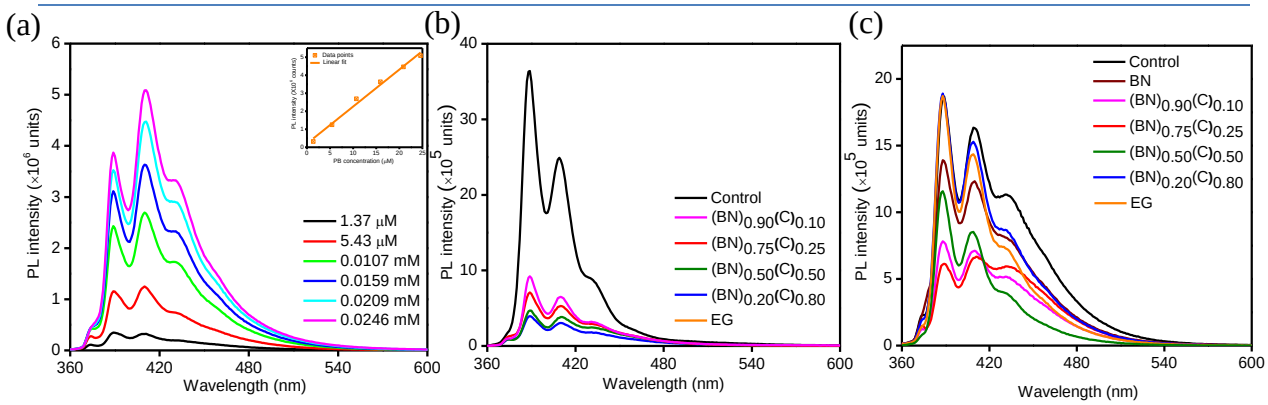

Figure 9: (a) Emission spectra of 1-(bromomoacetyl)pyrene (PB) of different concentrations (excitation wavelength 320nm) along with calibration plot at 410 nm (b) Emission spectra of PB reacted with carboxylic groups of EG and BCN along with the control experiment (c) Emission spectra of PB reacted with hydroxyl groups of EG, BN and BCN along with the control experiment

In addition to oxygen containing functionalities, BCN would contain amine functionality on the surface due to reaction of urea with graphene during synthesis. The number of these functionalities can vary with the composition due to variation in the number of graphene, BCN and BN domains with composition. BN is also expected to have amine surface groups. In order to probe the amine functionalities on BN and BCN surfaces, we have used the NHS-Cy5 as the fluorescent probe which is very specific to amine group. We have measured the florescence of various known concentrations of NHS-Cy5 with excitation at 530 nm as shown in Figure 10a with the corresponding calibration plot at 680 nm in the inset (**Figure** 10a). The FLOSS results of NHS-Cy5 reaction with the amine functional groups on BN and various compositions of BCN are shown in the **Figure** 10b. We have carried out control reactions without the reagent to rule out physisorption of dye molecules (**Figure** 10c).

Fluorescence results show that the carbonyl and carboxylic acid groups on the surface of BCN follows a linear trend with increasing carbon content. The number of amine groups on the surfaces increases with increase in carbon content. But the sample with highest carbon content $(BN)_{0.20}C_{0.80}$ shows deviation from the observed trend and possesses a less number of

amine groups compared to $(BN)_{0.50}C_{0.50}$. This can be attributed to the molar proportion of the aminating agent (urea) used to get $(BN)_{0.20}C_{0.80}$ composition is 10 times lesser than that of $(BN)_{0.50}C_{0.50}$. We do not observe any trend on the number of surface hydroxyl groups. The surface group quantification results have been summarised in **Table** 3

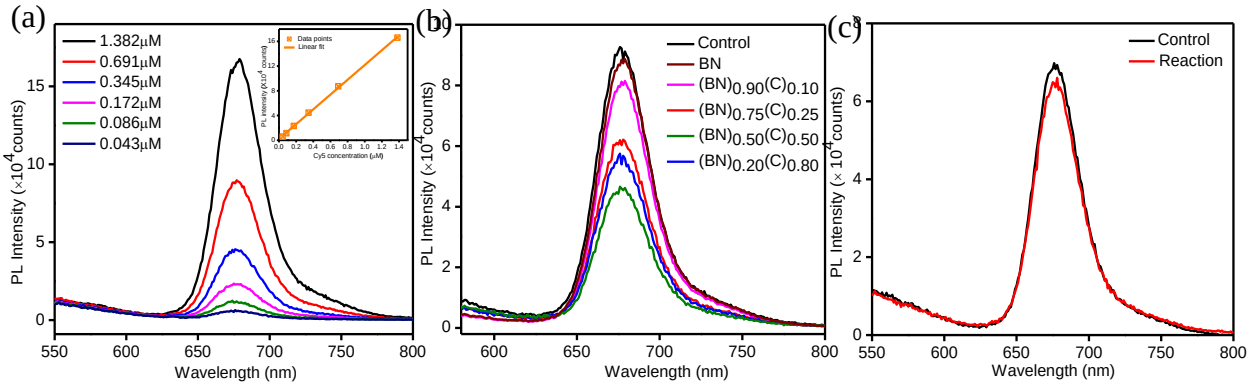

Figure 10: (a) Emission spectra of NHS-Cy5 of different concentrations (excitation wavelength 530nm) along with calibration plot at 680 nm (b) Emission spectra of NHS-Cy5 reacted with amine groups of BN and BCN along with the control experiment (c) Physisorption experiment for NHS-Cy5

Electrochemical measurements

We have studied supercapacitor performance and oxygen reduction reaction (ORR) activity of EG and BCN samples to look for the possible effects of surface groups on the electrochemical behaviour of these materials. Supercapacitor performance was investigated by means of cyclic voltammetry (CV), galvanostatic charge-discharge curves in 1 M H_2SO_4 aqueous electrolyte (**Figure**s 11a and b respectively). The quasi-rectangular CV curves indicate excellent charge storage capability. The highly symmetric charge-discharge plots also give indication of good charge storage capability. $(BN)_{0.75}C_{0.25}$ out performs all other samples (**Figure** 11c). The calculated specific capacitances (**Table** 2) for the BCN samples follow a similar trend as the number of surface amine groups.

The ORR electrocatalytic activity of EG and BCN samples in O_2-saturated 0.1 M KOH solution is shown in **Figure** 12a. BCN catalysts show cathodic peaks in the range -0.09 to -0.24 V, indicating good O_2 reduction property. Linear-sweep voltammetry (LSV) of BCN at a

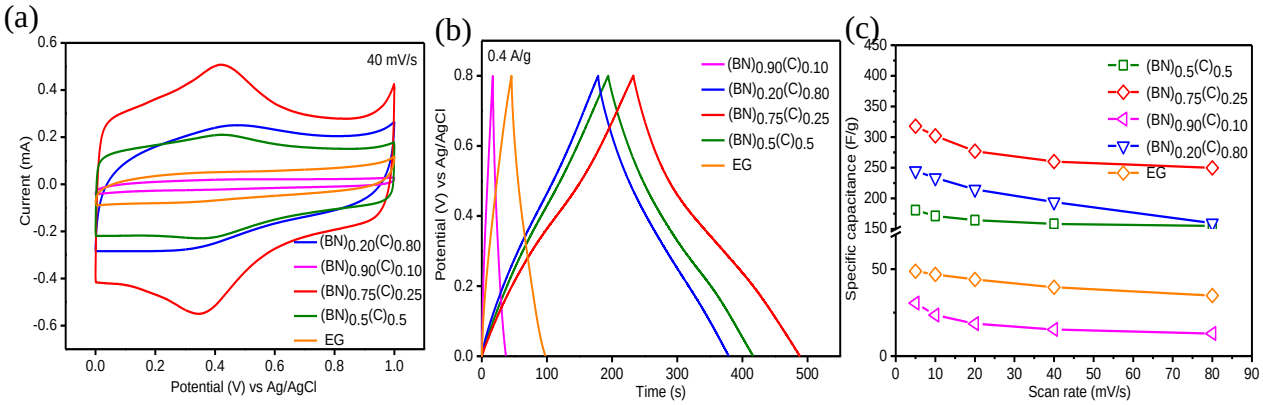

Figure 11: (a) Cyclic voltammetry curves of EG and BCN supercapacitor at a scan rate 40 mV/s in 1 M H_2SO_4 (b) galvanostatic charge–discharge curves at a current density of 0.4 A/g (c) Specific capacitance of EG and BCN samples as a function of scan rates

rotation speed of 1600 rpm was carried out on an RDE as shown in **Figure** 12b. $(BN)_{0.75}C_{0.25}$ shows the best ORR catalytic activity among other samples (**Figure** 12c). The order observed in the case of ORR also somehow follows the trend for amine functionalities.

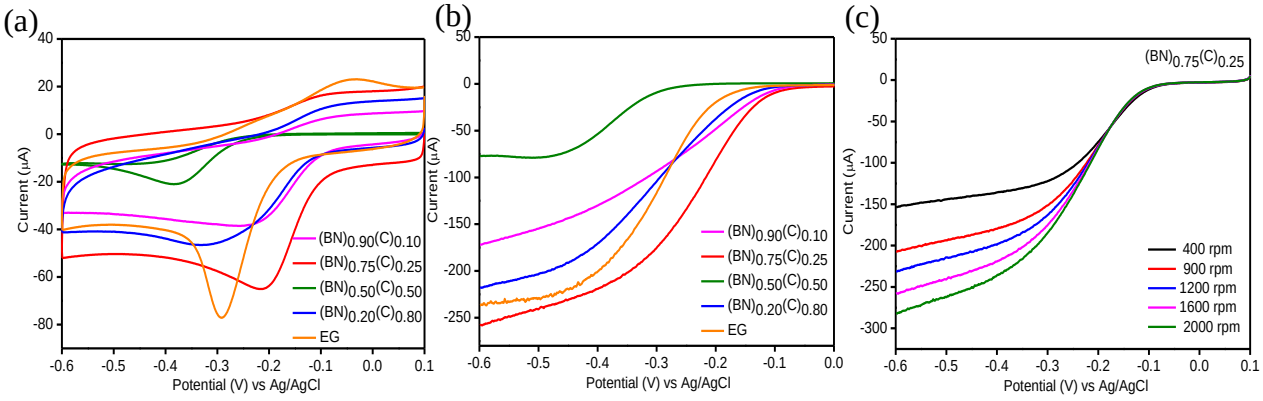

Figure 12: (a) cyclic voltammetry of EG and BCN samples at scan rate 20 mV/s in O_2 saturated 0.1 M KOH (b) LSV curves of BCN samples at a scan rate of 5 mV/s and rotation speed of 1600 rpm (c) LSV curves of $BN_{0.75}C_{0.25}$ at different rotations

Table 1: Compositions of BCN along with the molar ratios of the precursors used for synthesis

Composition	Boric acid (mg)	Urea (g)	Exfoliated graphene (g)
BN	100	1.000	-
$(BN)_{0.90}(C)_{0.10}$	500	5.000	0.050
$(BN)_{0.75}(C)_{0.25}$	150	1.500	0.050
$(BN)_{0.50}(C)_{0.50}$	50	0.500	0.050
$(BN)_{0.20}(C)_{0.80}$	5.5	0.055	0.050

Table 2: Surface area, specific capacitance and ORR onset potentials of EG and BCN

Composition	Surface area (m^2/g)	Specific capacitance (F/g)	ORR onset potential (V)
$(BN)_{0.90}(C)_{0.10}$	130	18	-0.10
$(BN)_{0.75}(C)_{0.25}$	254	276	-0.09
$(BN)_{0.50}(C)_{0.50}$	437	164	-0.24
$(BN)_{0.20}(C)_{0.80}$	454	240	-0.14
EG	948	44	-0.14

Table 3: Surface areas and FLOSS results of various surface functional groups on EG, BN and BCN

Composition	Surface area (m^2/g)	Carbonyl group (groups/g) (groups/cm^2)	Carboxyl group (groups/g) (groups/cm^2)	Hydroxyl group (groups/g) (groups/cm^2)	Amine group (groups/g) (groups/cm^2)
BN	142	-	-	2.94×10^{20} (20.70×10^{13})	0.04×10^{20} (0.03×10^{13})
$(BN)_{0.90}(C)_{0.10}$	190	0.97×10^{20} (5.10×10^{13})	23.44×10^{20} (123.37×10^{13})	10.38×10^{20} (54.63×10^{13})	0.44×10^{20} (2.31×10^{13})
$(BN)_{0.75}(C)_{0.25}$	254	1.33×10^{20} (5.24×10^{13})	25.45×10^{20} (100.20×10^{13})	11.51×10^{20} (45.31×10^{13})	1.36×10^{20} (5.35×10^{13})
$(BN)_{0.50}(C)_{0.50}$	437	1.80×10^{20} (4.12×10^{13})	27.36×10^{20} (62.61×10^{13})	8.95×10^{20} (20.48×10^{13})	2.15×10^{20} (4.92×10^{13})
$(BN)_{0.20}(C)_{0.80}$	454	2.08×10^{20} (4.58×10^{13})	28.81×10^{20} (63.46×10^{13})	0.03×10^{20} (0.07×10^{13})	1.71×10^{20} (3.77×10^{13})
EG	948	2.27×10^{20} (2.39×10^{13})	28.32×10^{20} (29.87×10^{13})	0.86×10^{20} (0.91×10^{13})	-

.

1.4 Conclusions

The present study demonstrates the success of FLOSS in quantifying surface functional groups on the surfaces of EG, BN and BCN. The FLOSS results on carbonyl, carboxylic and amine groups are satisfactory, but for hydroxyl groups the results may not be as reliable due to lack of chemoselectivity. The concentration of carbonyl and carboxylic groups increase with the carbon content in borocarbonitrides. The FLOSS is a reliable method for the quantification of surface amine groups as well. The BCN samples show good supercapacitor performance compared to graphene.

REFERENCES

1. Y. Xing, N. D., E. Borguet, *Curr. Opin. Solid State Mater. Sci.* **2007,** 11.
2. C.F. Chiu, N. D., E. Borguet, *J. Phys. Chem. A* **2011,** 115.
3. N. Dementev, X. F., E. Borguet, *Langmuir* **2009,** 25.
4. T. Pellenbarg, N. D., R. Jean-Gilles, C. Bessel, E. Borguet, N. Dollahon, R. Giuliano, *Carbon* **2010,** 48.
5. X. Feng, N. D., W. Feng, R. Vidic, E. Borguet, *Carbon* **2006,** 44.
6. Holländer, A., *Surf. Interface Anal.* **2004,** 36.
7. S.R. Holmes-Farley, G. M. W., *Langmuir* **1986,** 2.
8. C. Funk, P. M. D., T. Gross, H. Min, W.E.S. Unger, W. Weigel, *Surf. Interface Anal.* **2012,** 44.
9. V.B. Ivanov, J. B., A. Holländer, F. Mehdorn, H. Zimmermann, *Surf. Interface Anal.* **1996,** 24.
10. E.A. McArthur, T. Y., J.P. Cross, S. Petoud, E. Borguet *J. Am. Chem. Soc.* **2004,** 126.
11. C.N.R. Rao, K. G., *ACS Appl. Mater. Interfaces* **2016**.
12. M.B. Sreedhara, K. G., B. Bharath, R. Kumar, G.U. Kulkarni, C.N.R. Rao, *Chem. Phys. Lett.* **2016,** 657.
13. K.S. Subrahmanyam, S. R. C. V., A. Govindaraj, C.N.R. Rao, *J. Mater. Chem.* **2008,** 18.
14. W.S. Hummers, R. E. O., *J. Am. Chem. Soc.* **1958,** 80.
15. A. Nag, K. R., K.P.S.S. Hembram, R. Datta, U.V. Waghmare, C.N.R. Rao, *ACS Nano* **2010,** 4.
16. Y. Xing, E. B., *Langmuir* **2007,** 23.
17. A. Jana, S. A., S.K. Sarkar, N.D.P. Singh, *Tetrahedron* **2010,** 66.
18. B. Gong, B.-K. C., J.-Y. Kim, D. Shetty, Y.H. Ko, N. Selvapalam, N.K. Lee, K. Kim, *J. Am. Chem. Soc.* **2015,** 137.
19. E. Gallegos-Suarez, M. P.-C., A. Guerrero-Ruiz, I. Rodriguez-Ramos, A. Arcoya, *Appl. Surf. Sci.* **2013,** 287.
20. S. Flink, F. C. J. M. v. V., D.N. Reinhoudt, *Adv. Mater.* **2000,** 12.
21. S.W. Song, K. H., S. Kawi, *Langmuir* **2005,** 21.

22. H. Gong, S.-T. K., J.D. Lee, S. Yim, *Appl. Surf. Sci.* **2013,** 266.

23. H. Hu, P. B., B. Zhao, M.A. Hamon, M.E. Itkis, R.C. Haddon, *Chem. Phys. Lett.* **2001,** 345.

24. H.P. Boehm, E. D., W. Heck, R. Sappok, *Angew. Chem. Int. Ed.* **1964,** 3.

CHAPTER 2

Mechanical and thermal properties of borocarbonitrides nanosheet-reinforced polymer nanocomposites*

SUMMARY

The enhancement in the mechanical and thermal properties of polymer nanocomposites strongly depends on the extent of molecular-level interactions and interfacial adhesion between the nanofiller and the matrix material. The interaction is governed by the surface functionalities on the nanofiller. Herein, we examine the effect of nanosheets of borocarbonitides, $(BN)_xC_{1-x}$, which are analogues to graphene (x=0) and boron nitride (x=1), whose surface functional groups varies with the composition on the mechanical and thermal properties of poly(vinyl alcohol), PVA. Results show that substantial improvements in hardness and elastic modulus of PVA can be achieved by adding only 0.2 wt% of BCN. A significant enhancement in the thermal stability was also noted.

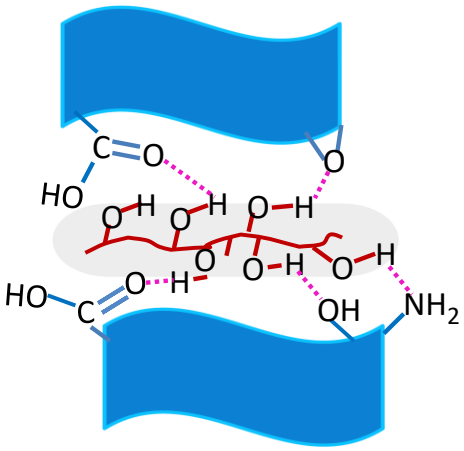

2.1 Introduction

A key attribute of nanomaterials is the substantial surface-to-volume ratio (STVR) they offer. The resultant alteration in the chemical and physical properties, as compared to the respective bulk properties, are not only scientifically interesting but can be exploited for engineering new materials and devices. One such class of materials are the polymer matrix composites (PMCs) reinforced with nanoparticles[1]. Because of their high STVR, even a small addition (typically less than 1 wt.%) of the nanofillers to the polymer matrix can result in a pronounced enhancement in latter's mechanical properties while traditional composites will need as much as 60 vol% reinforcement for similar enhancement in mechanical properties[2-4]. However, substantial benefits of nanocomposites can be accrued only when the fillers are properly dispersed in the polymer matrix such that proper interfacial interaction can take place between the filler and the polymer chains. In this context, the surface functional groups on the filler play a major part. However, major advantage of the nanofillers, namely STVR, is also the main impediment as agglomeration of the nanoparticles, so as to minimize their surface area, is a common occurrence.

It was successfully demonstrated that simultaneous addition of more than one type of nanofiller, especially those with differing dimensionality such as one dimensional nanotubes to two dimensional nanosheets (e.g. graphene), can lead to extraordinary synergy in enhancing the mechanical properties[5]. In the present work, we examine whether such synergistic benefits can also obtained in borocarbonitride, $(BN)_xC_{1-x}$, (BCN) nanosheet reinforced poly(vinyl alcohol), PVA, nanocomposites.

Nanosheets of BCN have attracted recent attention due to their exotic semiconducting properties, which could be tuned by varying the composition, i.e., boron nitride (BN)-to-

carbon ratio. Moreover, they offer a diverse set of surface functionalities, domain structures, and a high degree of chemical heterogeneity, which make them considerably more interesting than either graphene or BN. Keeping this in view, a number of studies have explored the potential applications of BCN nanosheets in batteries, supercapacitors, gas adsorption, and catalysis[6]. Given the exceptional mechanical properties of either graphene and BN reinforced based polymer nanocomposites[7], and the possibility of synergy, we expect that BCN polymer nanocomposites to exhibit excellent mechanical and thermal properties, particularly in view of the interesting chemical environments the BCN nanosheets offer. This possibility was investigated in this study through a detailed characterization of mechanical and thermal properties.

2.2 Experimental

Materials: Polyvinyl alcohol (Kemphasol, 14000 Da), water (Millipore)

Synthesis

Synthesis of nanofillers

Although it is possible to synthesize borocarbonitride (BCN) nanosheets by several methods[6], BCN obtained by using exfoliated graphene (EG) via solid state reaction [8]offers a rich variety of surface functional groups and also possess high surface area[9]. Hence, it has chances of being a better nanofilers. Keeping this in view, exfoliated graphene (EG) was prepared by thermal treatment of graphene oxide at 1050 °C under N_2 atmosphere. $(BN)_xC_{1-x}$ with x = 0.2, 0.5, 0.75, and 0.9, were prepared by solid state reaction. Briefly, EG, boric acid, and urea were dispersed in water using ultrasonication. Then, excess water is evaporated to make slurry, which was then heated at 900 °C for 5 h under N_2 atmosphere. The composition of BCN was varied by changing the boric acid /carbon ratio[8]. Boron nitride (BN) was prepared in a similar way as BCN using boric acid and urea.

Synthesis of Polymer nanocomposites

A homogeneous dispersion of the nanofillers within the polymer matrix can be achieved by using a common solvent with which both the polymer and BCN can interact simultaneously. Since semi-crystalline PVA is water soluble, and BCN is highly dispersible in water due to the polar surface groups in it, BCN-PVA nanocomposites were synthesized by using water as the solvent.

For preparation of polymer nanocomposites, 499 mg of polyvinyl alcohol (PVA) was dissolved in 40 mL water heated to 80 °C. 1 mg of BCN dispersed in 1 mL water-ethanol, was added to the PVA solution. The resulting solution was further sonicated for about 5 hours, while maintaining a bath temperature of ~ 70 °C such that the total volume of the liquid decreases by 75%. At this stage, the solution was poured into a petri dish, dried at an oven maintained at 55 °C for 72 hours and then desiccated for at least 72 hours prior to characterization and nanoindentation measurements. For comparison purposes, pure PVA and PVA reinforced with either EG or BN were also prepared by using identical processing steps. In all composites examined in this study, the amount of filler loading was fixed at 0.2 wt%. **Scheme** 1 gives a representation of the steps involved in the preparation of polymer nanocomposites.

Characterization

The morphologies of nanosheets and polymer matrix were characterized by using a field emission scanning electron microscope (FESEM) Nova NanoSEM 600 (FEI Company). The extent of dispersion of BCN nanosheets in PVA matrix was analysed by cross-sectional FESEM. The cross-sections for this purpose were obtained by fracturing the samples after dipping in liquid N_2 for ~600 s. X-ray diffraction (XRD) of the nanocomposites and PVA was

performed in a Panalytical diffractometer (Empyrean) using the monochromatic Cu $K\alpha_1$ radiation (λ = 1.54Å). Raman spectroscopy was conducted with a JobinYvonLabRam HR spectrometer equipped with a 514 nm Ar laser, in backscattering geometry. Transmission electron microscopy (TEM) was performed with a FEI Tecnai G2 S-Twin operated microscope, fitted with a Gatan CCD camera, at an accelerating voltage of 200 kV. Fourier transform infrared spectra (FTIR) were recorded in a Bruker FTIR spectrometer in ATR mode. Thermo-gravimetric analyses (TGA) were carried out in N_2 atmosphere with a Metler Toledo TGA-850 analyzer at the rate of 5 °C/min. Differential scanning calorimetry (DSC) measurements were carried out in TA instrument in N_2 atmosphere with the heating and cooling rate 3 °C/min.

Nanoindentation

The nanoindentation technique was utilized to evaluate the mechanical properties. For this, the Triboindenter system (Hysitron, Inc., Minneapolis, MN, USA), equipped with a cono-spherical tip of radius (*R*) 1 μm was used. The choice of this particular tip geometry was made, instead of a sharp tip like Vickers or Berkovich that are generally used for nanoindentation, so as to reduce the displacement at any given load[10]. In all cases, the loading and unloading rates were maintained at 0.5and 2mN/s respectively, and the peak load was 500 μN. Faster loading and even speedier unloading rates were utilized so as to reduce viscoelastic recovery and to avoid the typical 'knee' during unloading. These parameters further help in obtaining a convergent solution for the power law fit[11]. A hold time of 250 s at the peak load was used to avoid the creep effects that typically result in the overestimation of Young's modulus, *E*. To avert any inaccuracy in the calculation of depth, *h*, the area function file had been calibrated using Polycarbonate instead of conventionally used fused quartz[12]. The load, *P*-displacement curves generated through the following procedure were further

fitted using power law equation given by Oliver and Pharr to obtain the values of *E* and *H* (hardness)[13].

2.3 Results and discussion

Material characterization

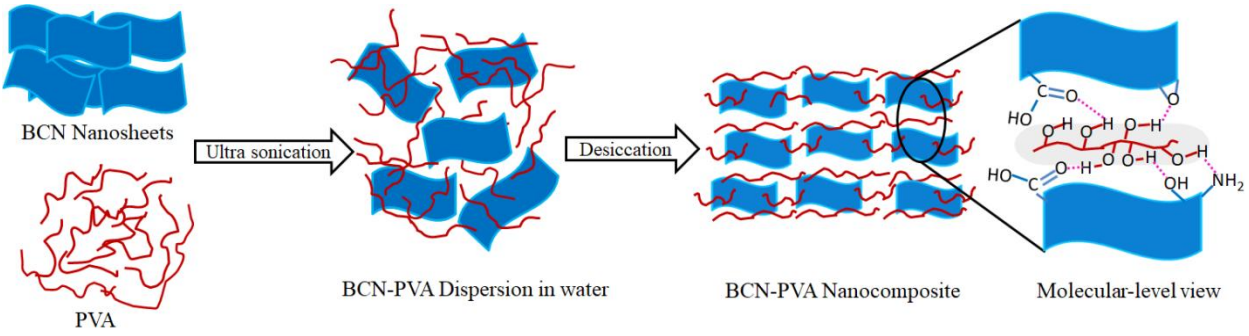

Scheme 1: Pictorial representation of BCN-PVA nanocomposite preparation and its molecular level view.

Schematic representations of EG, BCN and BN with their respective functional groups are displayed in **Figure**s 1a, 1b and 1c respectively. They illustrate the presence of multitude of active surface functional groups such as carboxylic acid, amine, carbonyl, epoxy, and hydroxyl groups, on the surfaces of these materials. **Figure**s 1d, 1e and 1f show the corresponding TEM images for EG, BCN and BN. The electron-transparent nanosheets have wrinkled morphology comprising few van der Waals layers. The lateral dimensions of these sheets are in microns, which is above the critical length required for an effective reinforcement.

Characterization of polymer nanocomposite

Scheme 1 shows the steps involved in the preparation of the BCN-PVA nanocomposites and their possible interaction at the molecular level. The polar functionalities present on the surface of the BCN can establish H-bonding with the hydroxyl groups present on PVA backbone[14-16] . Cross-sectional FESEm shows nanosheets embedded into PVA matrix

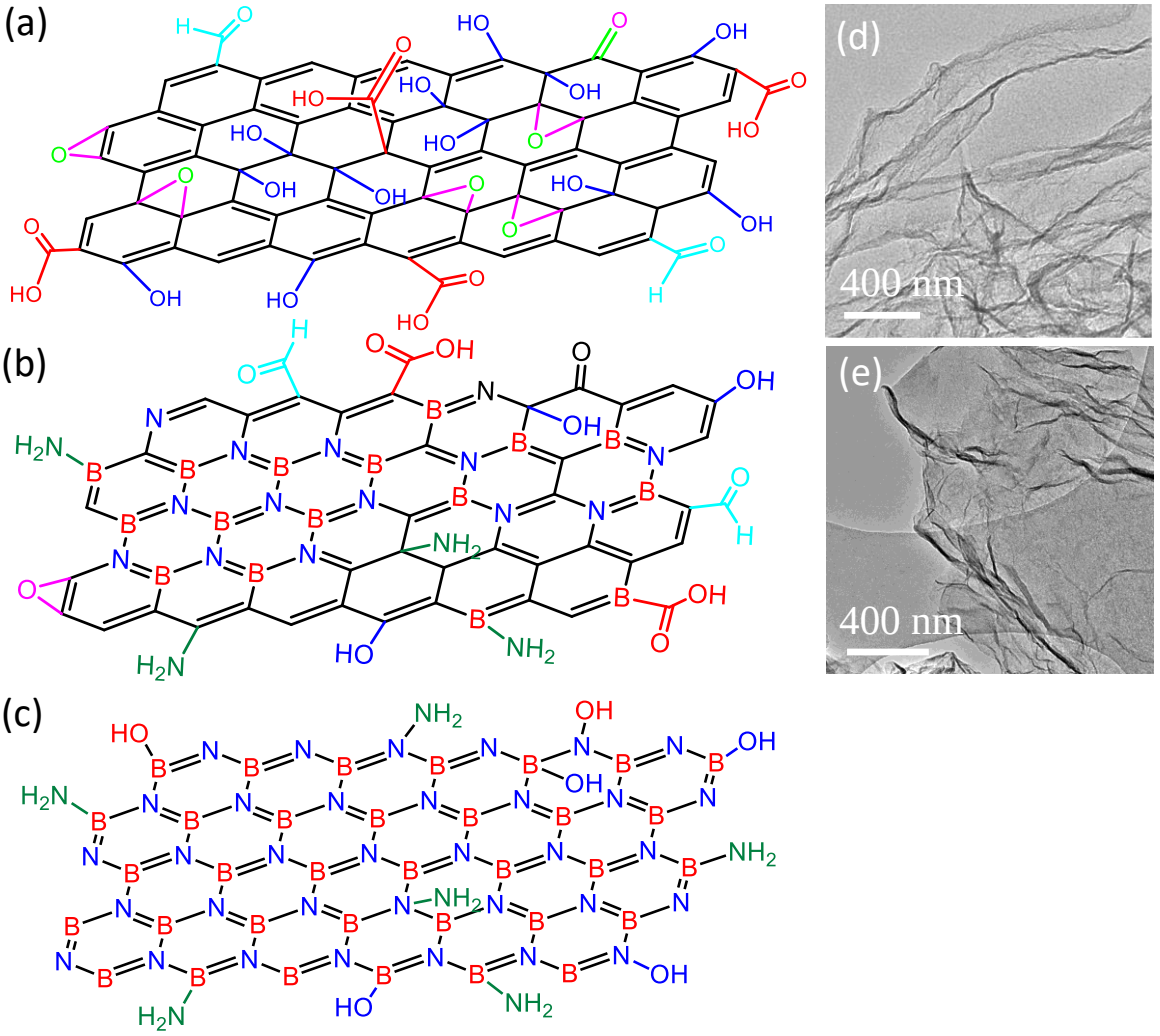

Figure 1: (a-c) schematic representations of EG, BCN and BN showing their surface functional groups respectively, (d-f) TEM images of EG, BCN and BN.

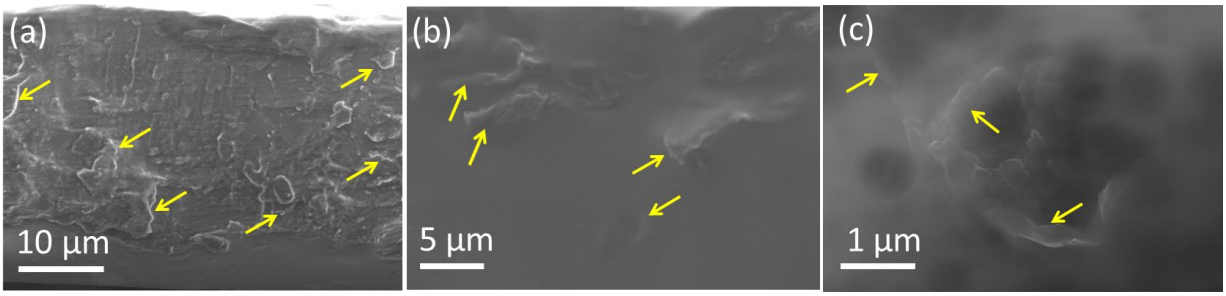

Figure 2: Cross-sectional FESEM images of BCN-PVA nanocomposite

XRD analysis provides valuable information regarding crystallinity, orientation and size of ordered regions within the polymer matrix. Representative XRD patterns obtained on pristine

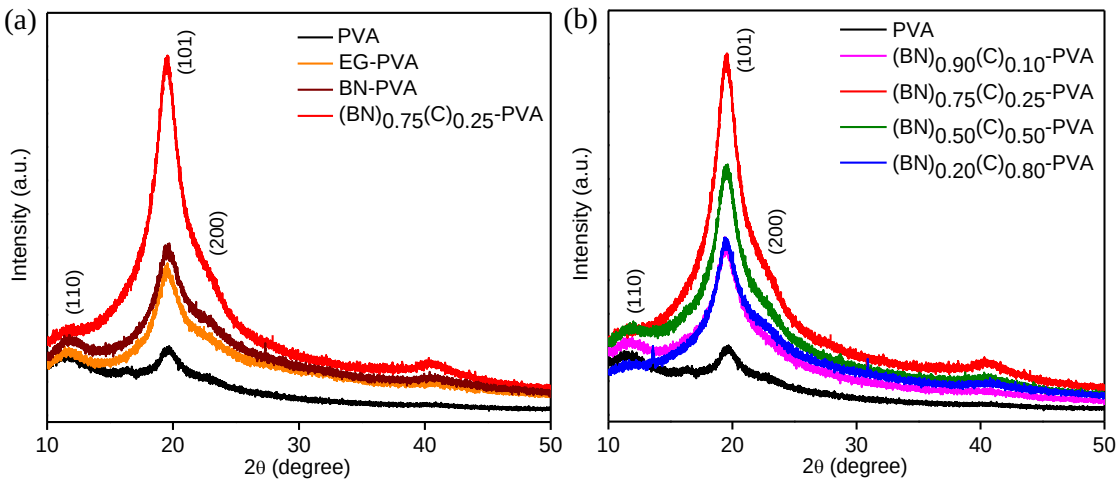

Figure 3: (a) X-ray diffraction patterns of PVA and $(BN)_{0.75}(C)_{0.25}$-PVA composites along with EG-PVA and BN-PVA loading of 0.2 wt% in comparison with for comparison (b) X-ray diffraction patterns of PVA and all BCN-PVA compositions

PVA, EG-PVA, BCN-PVA and BN-PVA nanocomposites are displayed in **Figure** 3a. In the base PVA, diffraction peaks at 11.5° and 19.5°, which correspond to diffractions from (110) and (101) planes respectively, give an indication of crystallinity in it. It is well known that the former, i.e., (101) diffraction peak of PVA, arises due to the intermolecular interference between PVA chains in the direction of the intermolecular hydrogen bonding. All the BCN nanocomposites also show strong (101) diffraction peaks, which give indication of higher crystallinity compared to pure PVA. This observation indicates that strong intermolecular H-bonding occurs between PVA and BCN as well as the interaction of the filler material facilitates crystal growth preferably along (101) plane. The ratios of the intensity of the Bragg peaks associated with (101) to (110) planes of the nanocomposites are much higher than that observed in pristine PVA, which indicates higher degree of crystallinity in the former. For example, $I_{(101)}/I_{(110)}$ is 4.208 in the nanocomposite reinforced with 0.2 wt.% $(BN)_{0.75}(C)_{0.25}$, whereas it is only 1.061 in pristine PVA. Slight shift in the 2θ value of (101) plane also indicate strong interaction of the filler material with PVA. Figure 3b shows the XRD patterns of all BCN-PVA nanocomposites along with PVA.

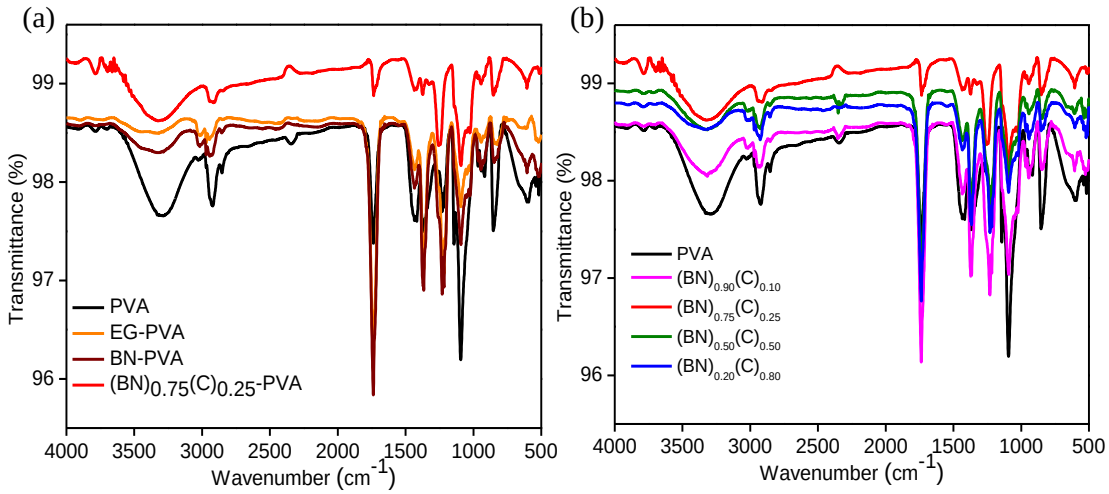

Figure 4: (a) FTIR spectra of PVA and $(BN)_{0.75}(C)_{0.25}$-PVA composites along with EG-PVA and BN-PVA (b) FTIR spectra of PVA and all BCN-PVA compositions

Figure 4a shows the FTIR spectra $(BN)_{0.75}(C)_{0.25}$-PVA nanocomposites in comparison to EG-PVA, BN-PVA along with pure PVA. The characteristic band at 3282 cm^{-1} in PVA corresponds to the hydroxyl group absorption on the polymer backbone. This band shifts to higher wave number upon the addition of nanofiller to PVA (**Figure**s 4a and 4b), which indicates stronger intermolecular interactions between BCN and PVA compared to hydrogen bonding within PVA.

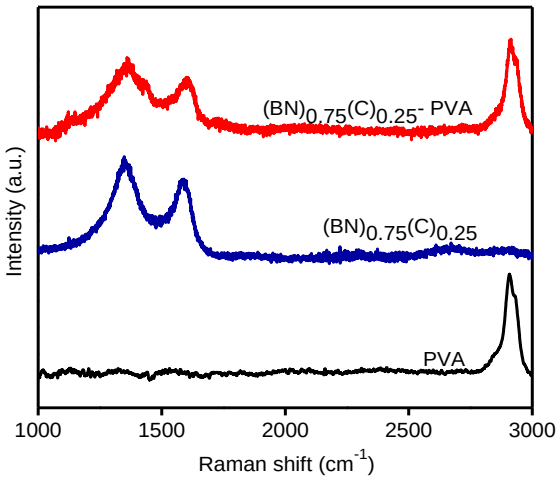

Figure 5: Raman spectrum PVA and PVA-BCN composites with the BCN loading of 0.2 wt% in comparison with pristine BCN (BCN composition is $(BN)_{0.75}(C)_{0.25}$

Raman spectra of the nanocomposites (**Figure** 5) show the characteristic bands at 1350 and 1560 cm^{-1}, which correspond to BCN nanosheets, and at 2900 cm^{-1} that corresponds to PVA's optical phonon mode. No significant difference in the spectra collected at different regions supports the conclusion about uniformity of nanosheet dispersion in the matrix

Mechanical properties of polymer nanocomposites

Mechanical properties measurements were carried out by Abhishek Chaturvedi and Upadrasta Ramamurty. Representative load displacement (*P-h)* responses obtained from nanocomposites of BN, $(BN)_{0.90}(C)_{0.10}$, $(BN)_{0.75}(C)_{0.25}$, $(BN)_{0.50}(C)_{0.50}$, $(BN)_{0.20}(C)_{0.80}$, and EG to PVA matrix are displayed in **Figure** 6a. Variations in the average values of *E* and *H*, extracted from these responses, with the composition are displayed in **Figure** 6b. For the unreinforced PVA, *E* and *H* are 4.2 ± 0.058 GPa and 76 ± 1.2 MPa, respectively which are

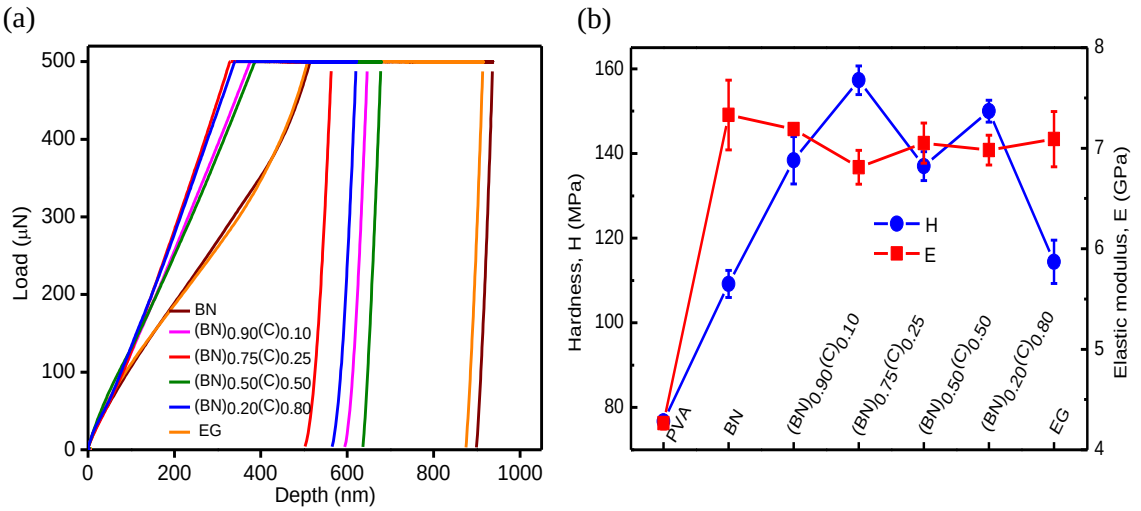

Figure 6: (a) Loading and unloading curves of EG to BN and BCN –PVA nanocomposites (b) variation of Hardness (*H*) and Elastic modulus (*E*) with composition in EG-PVA, BCN-PVA and BN-PVA nanocomposites

within the ranges of the respective values reported for PVA in literature[17]. **Figure** 6b shows that the addition of filler increases *E* to about 7 GPa, which is about 90% enhancement, irrespective of the filler material. The trends in *H* are different. The addition of either EG or

BN to PVA enhances it to either 114 ± 5.1 or 109 ± 3.2 MPa respectively, which are themselves substantial at ~50% and ~43% respectively. However addition of BCN to PVA, enhances *H* even further, with the $(BN)_{0.75}(C)_{0.25}$-PVA nanocomposite showing the highest *H* of 157 ± 3.4 MPA, i.e., more than double that of the base PVA.

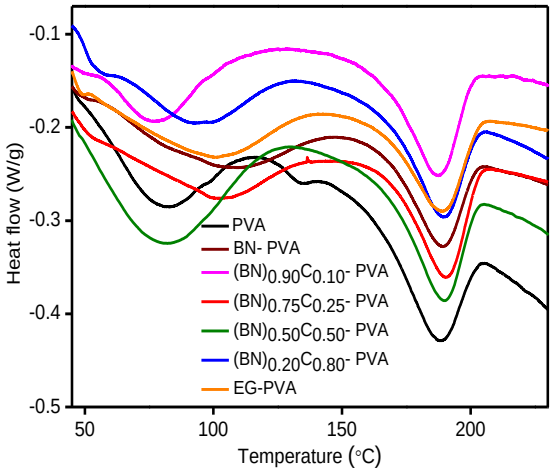

Figure 7: DSC scans of the different nanocomposites along with PVA

The substantial enhancement in the mechanical properties of the PVA upon the addition of nanofillers is possibly due to two factors: (i) an increase in the crystallinity within the polymer matrix and (ii) the reinforcement effect of the nanofillers that arises due to their substantially higher mechanical properties vis-a-vis PVA[18]. For the latter, an effective load transfer between the two constituent phases-the matrix and the nanofiller is essential, which strongly depends on the intermolecular H-bonding between PVA and BCN in the current context. Such a strong interaction restricts the mobility of the polymer chains, which, in turn, can alter the glass transition temperature (T_g) as well[19-21].

DSC is a suitable technique to determine both T_g and degree of crystallinity (χ) in a precise manner. The results of these experiments are displayed in **Figure** 7, which show that the T_g of PVA (~78 °C) increases to 96 °C upon the addition of $(BN)_{0.75}(C)_{0.25}$. The observed increase in T_g, which is substantial, indicates strong molecular interaction of polymer chains with filler. This was further substantiated with the observations on the crystalline melting

temperature (T_m). Both the pristine PVA and nanocomposites show T_m to be in the range of 180 to 200 °C; a slight increase in T_m of PVA on introduction of filler material suggests that it has a substantial effect on crystalline regions of PVA. Since PVA is a semi-crystalline polymer, a change in degree of crystallinity within it can alter its mechanical properties markedly. To examine this, we have plotted the variations of *H* and *E* (see **Table** 1) with χ in **Figure**s 8a and b. It reveals that *H* increases--nearly linearly—with χ. On the other hand, *E* doesn't show any linear trend with χ. These observations suggest that the enhancement in *E* that was noted in all the nanocomposites is not due to increase in χ. Hence, it must be due to the stress transfer mechanism from the matrix to reinforcement phase which is aided by the strong interface between those two phases[17, 22, 23].

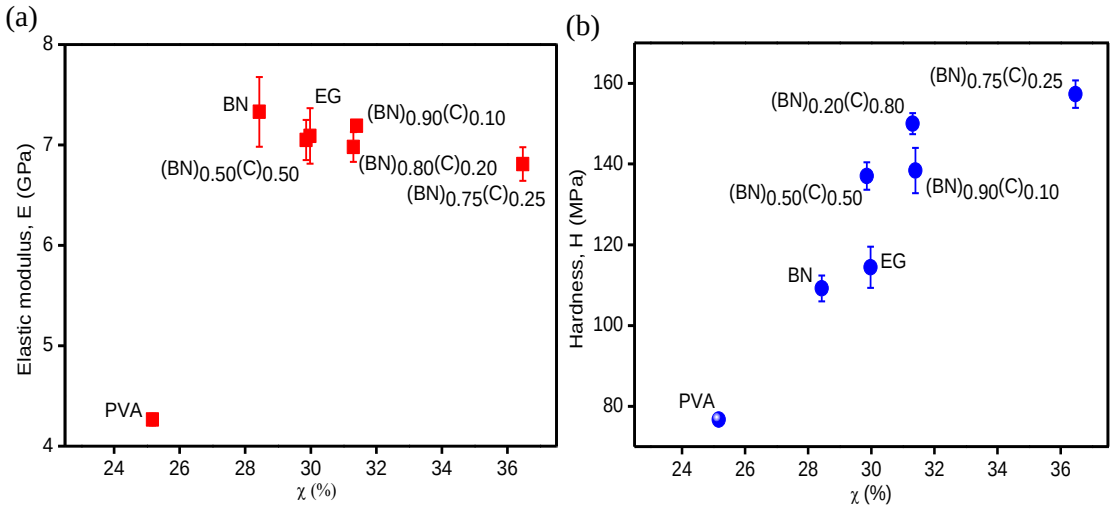

Figure 8: (a) Variation of *E* with χ (b) Variation of *H* with χ

Effective stress transfer leads to a substantially higher resistance to elastic deformation offered by the nanocomposites. This, in turn, results in the observed higher *E* of the nanocomposites. Furthermore, the results of XRD scans of the composites indicate that the filler material enhances the polymer chain alignment, with BCN nanosheets sequentially arranged parallel to the PVA chains. The presence of the surface functional groups aids this

process through strong intermolecular H-bonding. The alignment of the nanosheets and the presence of multitude of strong intermolecular interactions could be another reason for observed increase in *E*. Effective stress transfer leads to a substantially higher resistance to elastic deformation offered by the nanocomposites, which in turn results in higher *E* of the nanocomposites. Furthermore, the results of XRD scans of the composites indicate that the filler material enhances the polymer chain alignment, with BCN nanosheets sequentially arranged parallel to the PVA chains. The presence of the surface functional groups on the nanofiller aids this process through strong intermolecular H-bonding. The alignment of the nanosheets and the presence of multitude of strong intermolecular interactions could be another reason for observed increase in *E*.

The enhancements observed in *H*, in contrast to *E*, can be rationalized by recourse to the observed positive correlation between *H* and χ. Since the hardness of any material is a measure of its resistance to plastic deformation, it is instructive to briefly examine the micromechanisms of plasticity in semicrystalline polymers here. Typically, plasticity in these materials occurs, broadly, in four stages. They involve elongation of the chains that are in the amorphous regions, reorientation (or alignment) of the crystalline regions in the direction of the tensile stress, separation of crystalline units into chain-unfolded fibrillar structure, and finally tandem stretching of both the crystalline and amorphous regions. Since indentation made with a sharp tip involve large strains, the latter stages of deformation are especially relevant in the current context. Furthermore, the first two stages may not be that significant as such, given the high orientation that the BCN nanosheets induce within the polymers. Since the final stages are controlled by crystalline regions, we can infer that a polymer with a higher χ can offer considerably higher resistance to plastic deformation, which rationalizes the positive correlation found between *H* and χ in **Figure** 8a. Since the addition BCN to PVA

enhances the crystallinity in the latter, the substantially higher *H* in the nanocomposites can be attributed to the increased χ, which is facilitated by the presence of favorable surface functional groups in BCN and formation of newer nucleation sites owing to surface roughness of the fillers. Another very interesting observation was the variation of χ with composition (**Figure** 9). We observe that the trend is not linear and cannot be attributed to

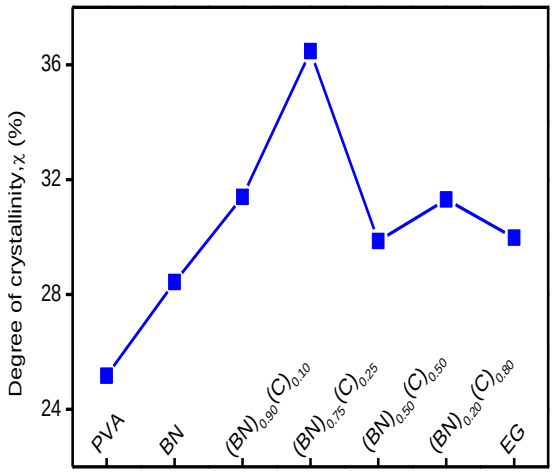

Figure 9: Variation of χ with composition

carbon content in the samples, surface area of the sample or the number of surface functional groups. Figure 9 however gives a clue that probably χ depends on the number of B-C-N domains because the number of B-C-N domains follow the same order as χ.

Thermal propertiesof polymer nanocomposites

Figure 10a and 10b show TGA scans and corresponding differential thermograms (DTG) of pure PVA and $(BN)_{0.75}(C)_{0.25}$-PVA nanocomposite. Both the polymer films undergo degradation by a two-step process. These correspond to the fragmentation of polymer backbone first and then complete decomposition of the polymer at a higher temperature. A substantial shift in the thermogram of the nanocomposite towards higher temperature (**Figure** 10b) gives indication of higher thermal stability of the nanocomposites which can be

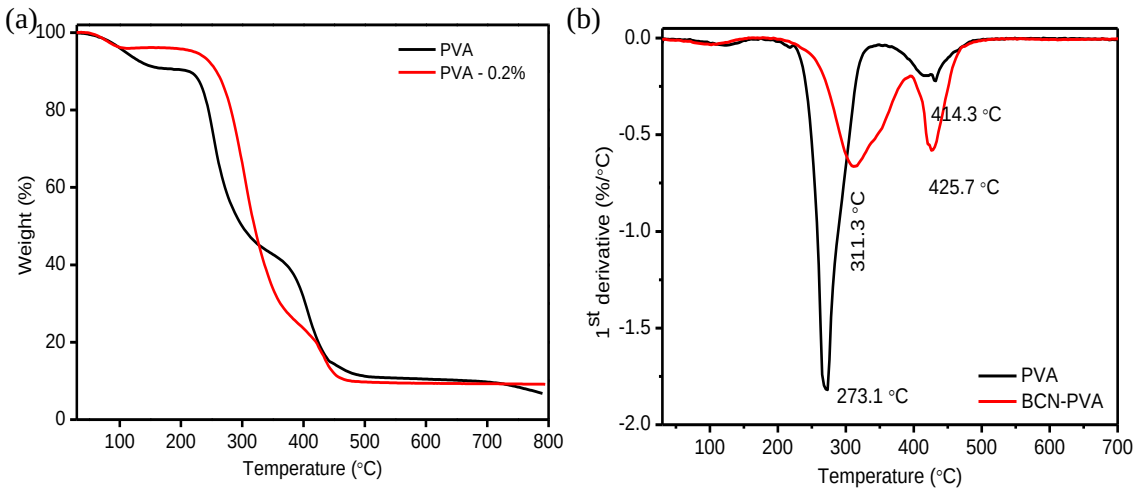

Figure 10: (a) TGA scans obtained on pure PVA and a PVA-BCN composite (b) corresponding DTG curve

to higher heat capacity of the BCN sheets and better barrier effects which retards the volatilization of polymer due to improved dispersion and interface.

Table 1: Mechanical properties of the different polymer nanocomposites

Nanocomposite	**Degree of crystallinity, χ (%)**	**Elastic modulus, E (GPa)**	**Hardness, H (MPa)**
PVA	25.17	4.265 ± 0.058	76.7 ± 1.2
BN	28.43	7.33 ± 0.347	109.2 ± 3.2
$(BN)_{0.90}(C)_{0.10}$	31.40	7.19 ± 0.038	138.4 ± 5.6
$(BN)_{0.75}(C)_{0.25}$	36.47	6.81 ± 0.168	157.3 ± 3.4
$(BN)_{0.50}(C)_{0.50}$	29.86	7.05 ± 0.200	137.0 ± 3.4
$(BN)_{0.20}(C)_{0.80}$	31.31	6.98 ± 0.148	150.0 ± 2.6
EG	29.98	7.09 ± 0.276	114.4 ± 5.1

2.4 Conclusions

In summary, polymer matrix nanocomposite of PVA with BCN as filler, were synthesized and characterized in detail. The high chemical heterogenity BCN and the method used for preparing it allows it to have high surface area and several surface functional groups, which, in turn, makes it an interesting filler material. These surface functionalities play a crucial role in the interfacial interaction between polymer and nanofiller via H-bonding. A 107% increment in hardness and 71% increment in elastic modulus were achieved by the addition of just 0.2 wt% of BCN to PVA. While the stiffness of the nanocomposites with varying chemical compositions of BCN are comparable with that of EG and BN nanocomposites, the hardness of the former are far superior to those reinforced with either BN or EG. The substantial improvement in the mechanical properties upon addition of nanofiller can be attributed to increase in crystallinity of the semi-crystalline polymer due to formation of newer nucleation centers owing to surface roughness of the filler and effective load transfer between the polymer matrix and the nanofiller, aided by H-bonding. Furthermore, BCN reinforced PVA films have higher thermal stability as compared to pristine PVA. Hence, BCN nanosheets are superior reinforcement material for enhancing the mechanical and thermal properties of polymers as compared to well-studied graphene and BN. Also, BCN can be produced economically compared to nanotubes and other kinds of nanocarbons.

REFERENCES

1. Njuguna, J. P., K.; Desai, S. , Nanofiller-Reinforced Polymer Nanocomposites. *Polym. Adv. Technol.* **2008,** 19.

2. Keller, T., Recent All-Composite and Hybrid Fibre-Reinforced Polymer Bridges and Buildings. *Prog. Struct. Mater. Eng* **2001,** 3.

3. Liu, P. J., Z.; Katsukis, G.; Drahushuk, L. W.; Shimizu, S.; Shih, C.-J.; Wetzel, E. D.;; Taggart-Scarff, J. K. Q., B.; Van Vliet, K. J.; Li, R.; Wardle, B. L.; Strano, M. S., Layered and Scrolled Nanocomposites with Aligned Semi-Infinite Graphene Inclusions at the Platelet Limit. *Science* **2016,** 353.

4. Ramanathan, T. A., A. A.; Stankovich, S.; Dikin, D. A.; Herrera-Alonso, M.; Piner, R.;D.; Adamson, D. H.; Schniepp, H. C.; Chen, X.; Ruoff, R. S.; Nguyen, S. T.; Aksay, I. A.; Prud'Homme, R. K.; Brinson, L. C. , Functionalized Graphene Sheets for Polymer Nanocomposites. *Nat. Nanotechnol.* **2008,** 3.

5. Prasad, K. E. D., B.; Maitra, U.; Ramamurty, U.; Rao, C. N. R., Extraordinary Synergy in the Mechanical Properties of Polymer Matrix Composites Reinforced with 2 Nanocarbons. *PNAS* **2009,** 106.

6. Rao, C. N. R. G., K. , Borocarbonitrides, Bxcynz: Synthesis, Characterization and Properties with Potential Applications. *ACS Appl. Mater. Interfaces* **2017,** 9.

7. Jan, R. M., P.; Bell, A. P.; Habib, A.; Khan, U.; Coleman, J. N., Enhancing the Mechanical properties of BN Nanosheet-Polymer Composites by Uniaxial Drawing. *Nanoscale* **2014,** 6.

8. Sreedhara, M. B. G., K.; Bharath, B.; Kumar, R.; Kulkarni, G. U.; Rao, C. N. R. , Properties of Nanosheets of 2d-Borocarbonitrides Related to Energy Devices, Transistors and Other Areas. *Chem. Phys. Lett.* **2016,** 657.

9. Barua, M. S., M. B.; Pramoda, K.; Rao, C. N. R. , Quantification of Surface Functionalities on Graphene, Boron Nitride and Borocarbonitrides by Fluorescence Labeling. *Chem. Phys. Lett.* **2017,** 683.

10. Klapperich, C.; Komvopoulos, K.; Pruitt, L., Nanomechanical Properties of Polymers Determined From Nanoindentation Experiments. *J. Tribol.* **2000,** 123, (3), 624-631.

11. Kadambi, S. B.; Pramoda, K.; Ramamurty, U.; Rao, C. N. R., Carbon-Nanohorn-Reinforced Polymer Matrix Composites: Synergetic Benefits in Mechanical Properties. *ACS Appl. Mater. Interfaces* **2015,** 7, (31), 17016-17022.

12. Briscoe, B. J.; Fiori, L.; Pelillo, E., Nano-indentation of polymeric surfaces. *JJ. Phys. D: Appl. Phys.* **1998,** 31, (19), 2395.

13. Oliver, W. C.; Pharr, G. M., An improved technique for determining hardness and elastic modulus using load and displacement sensing indentation experiments. *J. Mater. Res.* **2011,** 7, (6), 1564-1583.

14. Chen, J. G., Y.; Liu, W.; Shi, X.; Li, L.; Wang, Z.; Zhang, Y.; Guo, X.; Liu, G.; Li, W.; Beake, B. D., The Influence of Dehydration on the Interfacial Bonding, Microstructure and Mechanical Properties of Poly(Vinyl Alcohol)/Graphene Oxide Nanocomposites. *Carbon* **2015,** 94.

15. Hong, P.-D. C., J.-H.; Wu, H.-L., Solvent Effect on Structural Change of Poly(Vinyl Alcohol) Physical Gels. *J. Appl. Polym. Sci.* **1998,** 69.

16. Zhu, Y. W., H.; Zhu, J.; Chang, L.; Ye, L., Nanoindentation and Thermal Study of Polyvinylalcohol/Graphene Oxide Nanocomposite Film through Organic/Inorganic Assembly. *Appl. Surf. Sci.* **2015,** 349.

17. Cadek, M. C., J. N.; Barron, V.; Hedicke, K.; Blau, W. , Morphological and Mechanical Properties of Carbon-Nanotube-Reinforced Semicrystalline and Amorphous Polymer

Composites. *J. . Appl. Phys. Lett.* **2002,** 81.

18. Schadler, L. S. G., S. C.; Ajayan, P. M., Load Transfer in Carbon Nanotube Epoxy Composites. *Appl. Phys. Lett.* **1998,** 73.

19. Barun, D. P., K. E.; Ramamurty, U.; Rao, C. N. R., Nano-Indentation Studies on Polymer Matrix Composites Reinforced by Few-Layer Graphene. *Nanotechnology* **2009,** 20.

20. Liang, J. H., Y.; Zhang, L.; Wang, Y.; Ma, Y.; Guo, T.; Chen, Y. , Molecular-Level Dispersion of Graphene into Poly(Vinyl Alcohol) and Effective Reinforcement of Their

Nanocomposites. *Adv. Funct. Mater.* **2009,** 19, 2297.

21. Mohsin, M. H., A.; Haik, Y. , Thermal and Mechanical Properties of Poly(Vinyl Alcohol) Plasticized with Glycerol. *J. Appl. Polym. Sci.* **2011,** 122.

22. Coleman, J. N. C., M.; Blake, R.; Nicolosi, V.; Ryan, K. P.; Belton, C.; Fonseca, A.; Nagy, J. B.; Gun'ko, Y. K.; Blau, W., High Performance Nanotube-Reinforced Plastics: Understanding the Mechanism of Strength Increase. *J. Adv. Funct. Mater.* **2004,** 14.

23. Gong, L. K., I. A.; Young, R. J.; Riaz, I.; Jalil, R.; Novoselov, K. S., Interfacial Stress Transfer in a Graphene Monolayer Nanocomposite. *Adv. Mater.* **2010,** 22.

CHAPTER 3

2D phosphorene nanosheets and quantum dots and their interaction with electron donor and acceptor molecules*

SUMMARY

Phosphorene, a two-dimensional material, has been a subject of recent investigations. An important aspect of phosphorene is whether holes and electrons can both be doped in this material. We have carried out an investigation of chemical doping of phosphorene by a variety of electron donor and acceptor molecules, employing both experiment and theory. We have also synthesized blue fluorescent phosphorene quantum dots with average particle sizes of ~5nm and studied its quantum yield and quenching of fluorescence in presence of organic donors and acceptors.

**A paper related to this work has appeared in ChemPhysChem (2017) and another manuscript submitted*

3.1 Introduction

Phosphorene is a 2D analogue of graphene, but with a puckered honeycomb structure where three sp^3 hybridized phosphorus atoms are covalently linked[1]. The monolayer phosphorene has a direct band-gap around 0.3-1.45 eV exhibiting high carrier mobility with potential applications[2-5]. One of the properties of phosphorene that has aroused much interest in the recent times is the possibility of charge-transfer doping. However in literature there is a lot of anomaly regarding the type of doping favoured in phosphorene[6-11]. We have carried out charge-transfer doping of phosphorene using organic acceptors and donors like tetracyanoethylene (TCNE), and tetrathiafulvalene (TTF) and also with other aromatic acceptors and donors denoted by A2 and D2 in the text.

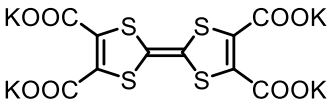

D2

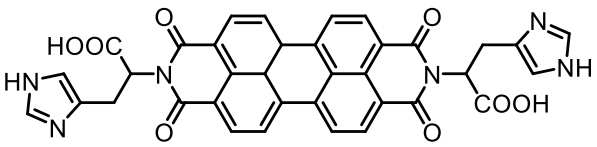

A2

Recently, there have also been a few reports on black phosphorus (BP) quantum dots, prepared by liquid exfoliation[10, 12, 13], pulsed laser ablation[14], or solvothermal methods[15]. Intense PL emission in the blue-violet region has been reported in the case of QDs prepared by pulse laser deposition in diethyl ether. However, the emission band position does not change with the excitation wavelength. This has been attributed to saturation passivation on the periphery and surfaces of the QDs by functional groups. Blue-green fluorescence has been obtained in QDs, prepared by a sonication assisted solvothermal method. We have therefore carried out the synthesis of phosphorene and studied the nature of charge-transfer doping preferred. We have also synthesized phosphorene quantum dots studied their

photoluminescence and other aspects. We have carried out first-principles calculations to understand the processes.

3.2 Experimental

Materials

Black phosphorous crystals (Smart elements, UK), *N*-Methyl-2-pyrrolidone (Sigma-Aldrich), N,N′-dimethylformamide (Spectrochem, India), Toluene (Sigma-Aldrich) and Mesitylene (Sigma-Aldrich) were purchased from commercial sources and used as received.

Synthesis

Synthesis of phosphorene

Phosphorene was synthesized by liquid exfoliation of black phosphorous (BP) crystals in NMP or DMF. Anhydrous NMP/DMF was purged with N_2 gas for 2 hours to remove dissolved oxygen. BP crystals were stored in an MBraun N_2 glove box with O_2 and H_2O levels of < 1.0 ppm. The BP crystals were ground into thin flakes. 20 mg of BP crystals were taken in a 50 mL centrifuge tube fitted with the probe sonicator tip to its cap. 20 mL of deoxygenated NMP/DMF was added to this vessel. The above steps were carried out in N_2 atmosphere as BP crystals are very sensitive to O_2. This centrifuge with the probe sonicator tip was then connected to sonicator operating at 20% amplitude and 20 kHz, 4 sec on / 4 sec off pulses for 4 hours. The set-up is connected to a chiller maintained maintained -2 °C. After sonication, the BP dispersion was centrifuged at 2000 rpm for 20 minutes. The supernatants were collected and further centrifuged at 5000 rpm for 1 hour. The light yellow supernatants were stored under nitrogen environment in a Schlenk flask.

Samples for Raman studies were prepared by sonication of phosphorene and donor/acceptor compounds. Typically, an aliquot amount of the solution of respective donor/acceptor compound was mixed with 50 μL of as-prepared phosphorene dispersion and bath sonicated for 2 hours. After sonication, the mixture was drop casted on glass slide and dried at 150 ^{O}C in an oven. The samples were vacuum dried in case of TCNE and TTF.

For ITC experiments, phosphorene dispersion was taken in the sample cell of the isothermal titration calorimeter and the reference cell filled with DMF. 10 μM solutions of tetracyanoethylene (TCNE), and tetrathiafulvalene (TTF) were prepared in DMF. The experiments were carried out at a constant temperature of 24 °C. Control experiments were performed by titrating the respective molecules against DMF under the same conditions, and the data so obtained were subtracted from the experimental data to eliminate the dilution effect.

Synthesis of phosphorene quantum dots

PQDs were prepared in dry and degassed toluene by probe sonication. 20 mg of BP crystals were taken in a 50 mL centrifuge tube fitted with the probe sonicator tip to its cap. Anhydrous toluene purged with N_2 gas was added into this centrifuge tube under N_2 atmosphere. The vessel was immersed in a water bath and connected to sonicator which was operated at 150 Watt and 4 sec on/ 4 sec off pulses for 8 hours. The water bath was cooled continuously throughout the exfoliation process by Julabo recirculating cooler. The gray dispersion obtained was centrifuged at 10000 by two cycles of 1 hour each to remove non-exfoliated BP particles. The supernatants were collected and stored under nitrogen in a Schlenk flask. Similarly PQDs were prepared by applying sonication power of 187.5 and 225 Watt in toluene and mesitylene.

Quantum yield measurements

Quantum yields were determined relative to quinine sulfate by using following formula.

$$\phi_{PQD} = \phi_{\text{quinine sulphate}} \left(\frac{\text{slope}_{PQD}}{\text{slope}_{\text{quinine sulphate}}} \right) \left(\frac{\eta^2_{\text{toluene}}}{\eta^2_{0.1\ \text{M}\ H_2SO_4}} \right)$$

where ϕ_{PQD} = fluorescence quantum yield (ϕ for quinine sulphate standard in 0.1 M H_2SO_4 = 54%), η = refractive index (toluene = 1.4869 and 0.1 M H_2SO_4 = 1.33), $\text{Slope}_{\text{quinine sulphate}}$ = 6.25×10^8 , Slope_{PQD} = 9.07×10^7, 7.04×10^7 and 7.36×10^7 for PQDs prepared at 150, 187.5 and 225 W respectively.

Four different samples of each PQD (in dry toluene) and quinine sulfate (in 0.1 M H_2SO_4) were prepared. To ensure the linearity of the integrated fluorescence intensities with optical densities, the absorbance at 360 nm was adjusted below 0.1 for all the samples by dilution. The wavelength integrated fluorescence intensities of various samples of PQD and quinine sulfate were plotted against their optical densities, giving rise to a linear plot. The slope values of these plots were substituted in the above equation to calculated fluorescence quantum yield.

Other details

Liquid exfoliation was carried out using a probe sonicator (Sonics Vibra cell™ VCX 750Ultrasonic processor). Raman spectroscopic studies were conducted by using a LabRAM HR high-resolution Raman spectrometer (Horiba-Jobin Yvon) using an Ar laser (λ = 514.5 nm). Transmission Electron Microscope (TEM) images were collected using a JEOL-3010 and FEI Titan3^{TM} with an accelerating voltage of 80 kV. Atomic Force Microscope (AFM) images were collected with a Bruker Innova Microscope. Absorption and photoluminescence (PL) spectra were recorded with a Perkin–Elmer UV/VIS/NIR lambda-750 and a Horiba–

Jobin–Yvon (*i*HR 320) spectrometers respectively. Isothermal calorimetry (ITC) measurements were carried out using a MicroCal VP-ITC unit

Computational details

Density Functional Theory based calculations for phosphorene were performed using Vienna Ab initio Simulation Package (VASP). To describe the exchange and correlation of electrons Perdew-Burke-Ernzerhof (PBE) functional within the generalized gradient approximation (GGA) has been considered[16]. Projected augmented-wave (PAW) potential has been used in all the calculations[17, 18]. A plane wave basis set with a sufficient energy cutoff of 500 eV has been used to represent valence electrons. To avoid the spurious interactions in the non-periodic direction, we created a vacuum of 30 Angstrom along the non-periodic direction and our supercell consideration keeps the molecules 10 Å away from each other. The systems are optimized until the forces acting on per atom are less than 0.02 eV/Å. We have considered the sampling of the Brillouin zone using a Monkhorst Pack grid of 5 X 5 X 1, and for the electronic property calculations, we have considered a 21 X 21 X 1 grid. For the Raman mode of molecules, we have used Gaussian 09 software package.

First-principles based Density Functional Theory calculations for PQDs have been performed in SIESTA (Spanish Initiative for Electronic Simulation with Thousands of Atoms) Package[19], and Gaussian 16 software[20]. To study the absorption spectra of black phosphorene PQDs of varying sizes, Siesta package was used with a plane wave basis set having energy cutoff of 400 Ry to describe all the systems, along with PAW (Projected Augmented Wave) potentials. Interelectronic correlations and exchange were treated with PBE (Perdew-Burke-Ernzerhorf) functionals as implemented in the GGA (Generalized Gradient Approach) method. The Brillouin zone was sampled with a 5 x 5 x 1 Monkhorst Pack grid. All systems were optimized until the total force reduced to 0.02 eV/atom. A vacuum of 30 Angstroms

was maintained in the non-periodic direction to prevent deluding interlayer interactions and the supercell length was chosen to be 15 Angstroms to avoid coulombic interactions in the periodic direction. Charge-transfer interactions with donor and acceptor molecules, namely TTF (tetrathiafulvalene) as the electron donating moiety and TCNE (tetracyanoethylene) and TCNQ (tetracyanoquinodimethane) as electron accepting groups with phosphorene PQD were studied using Mulliken Population Analysis.

3.3 Results and discussion

Phosphorene

Material characterization

Phosphorene was prepared from black phosphorous (BP) by liquid exfoliation in NMP/DMF (**Scheme** 1). The as synthesized phosphorene was characterized by transmission electron

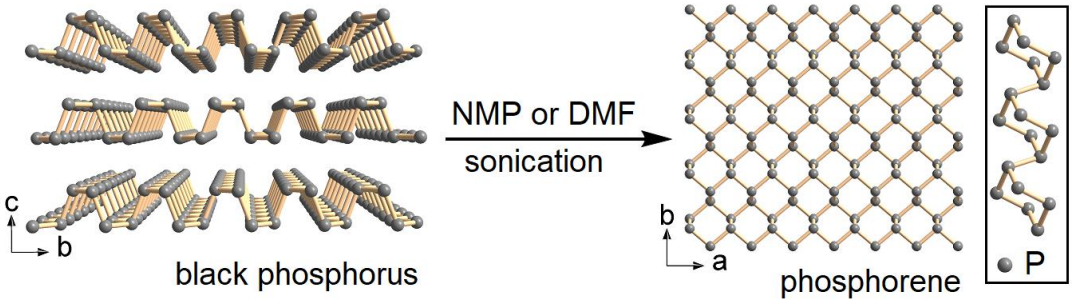

Scheme 1: Schematic representation of exfoliation of phosphorene from BP

microscopy, atomic force microscopy and Raman spectroscopy. **Figure** 1a shows the SEM image of layered BP while **Figure** 1b shows the Raman spectra of phosphorene along with that of BP. Raman spectra of phosphorene shows three Raman active modes A_g^1, A_g^2 and B_{2g} modes, inset shows the respective vibration modes. **Figure** 1c shows a typical TEM image of phosphorene while **Figure** 1d shows its HR-TEM image with atomic resolution. **Figure**s 1e and 1f shows the AFM image of phosphorene along with the corresponding height profile.

Charge transfer interaction with TCNE and TTF

Interaction of phosphorene with tetrathiafulvalene (TTF) and tetracyanoethylene (TCNE) which are classic donor and acceptor molecules respectively has been carefully studied using Raman spectroscopy and Isothermal titration calorimetry (ITC). **Figure** 2 shows the Raman spectra of phosphorene on interaction with TTF and TCNE. We observe softening of the A_g^1, A_g^2 and B_{2g} Raman bands on interaction with both TTF and TCNE. Along with softening, we observe band broadening as well in graphene[21, 22]. **Figure** 3 shows plots of the shift of the phonon frequencies ($\Delta\omega$) and the full width at half maxima (FWHM) with varying concentrations of TCNE and TTF respectively.

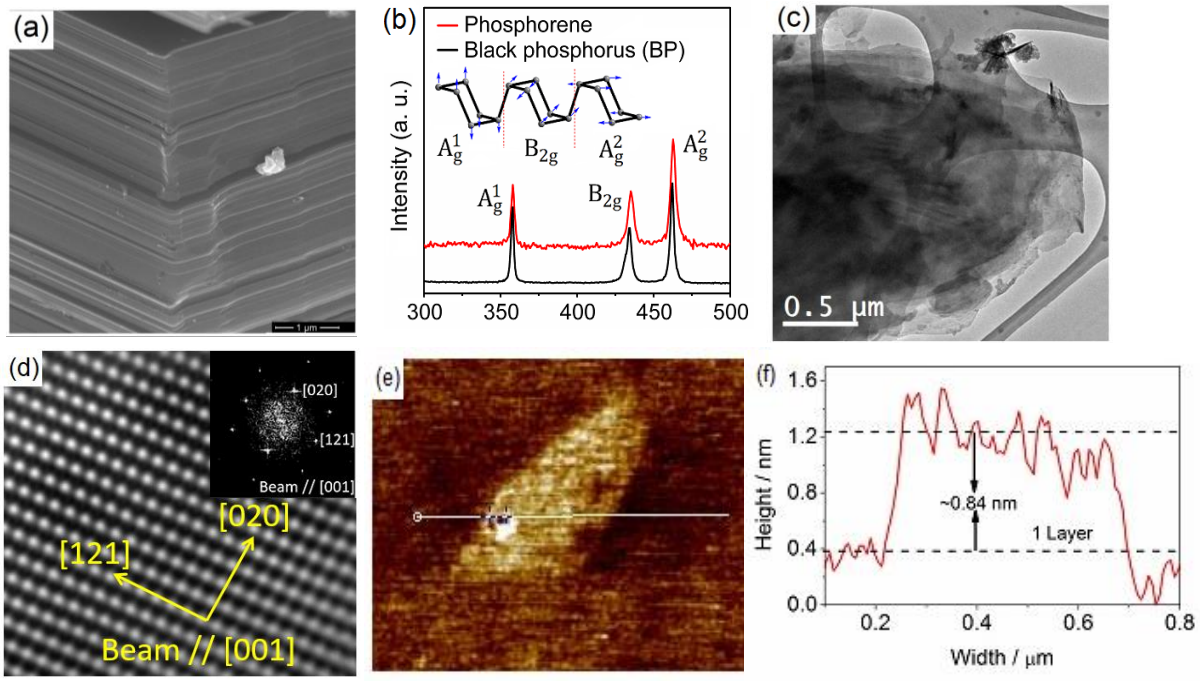

Figure 1: (a) SEM of black phosphorous (b) Raman spectra of phosphorene (c-d) TEM images of phosphorene (e-f) AFM image of phosphorene along with the corresponding height profile

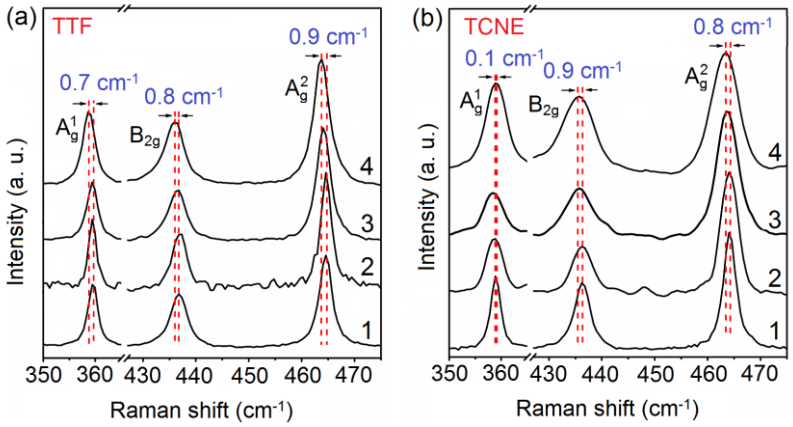

Figure 2: Raman bands of phosphorene on interaction with varying concentrations of (a) TTF (**1**; 0.0, **2**; 0.4, **3**; 0.8 and **4**; 1.6 mM) and (b) TCNE (**1**; 0.0, **2**; 0.4, **3**; 0.8 and **4**; 1.2 mM)

It should be noted that the changes in the Raman spectra caused by the interaction with donor and acceptor molecules arise mainly due to phonon-electron coupling just as in the case of graphene[6, 21]. Band broadening is slightly more with TCNE than TTF. TCNE also shows greater softening of the B_{2g} and A_g^2 bands and marginal softening of the A_g^1 band. Unlike with TCNE, softening of all the three bands is comparable in the case of TTF. These observations clearly show the absence of electron-hole asymmetry, although interaction with the acceptor TCNE, has a greater effect on the Raman spectra.

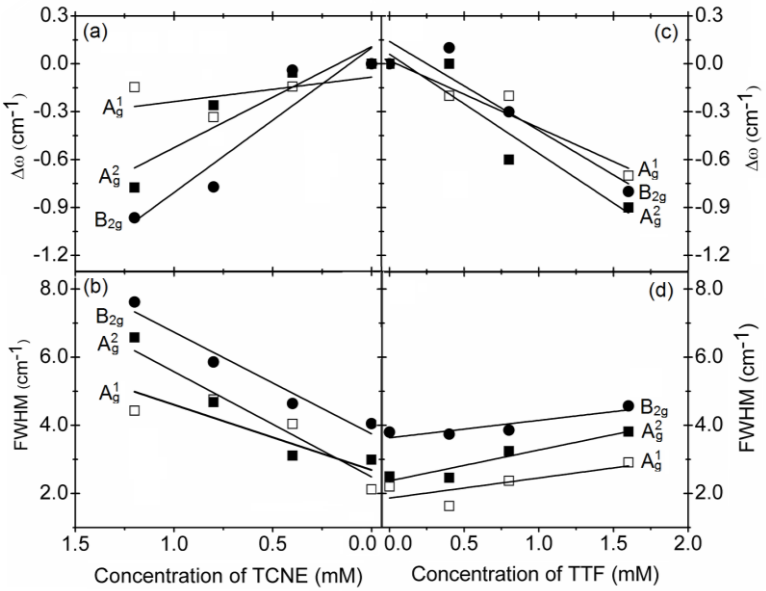

Figure 3: Shifts of the phonon frequencies (Δω) and the full width at half maxima (FWHM) of A_g^1, B_{2g} and A_g^2 bands of phosphorene as the function of concentration of (a-b) TCNE and (c-d) TTF. Increase in concentration of TCNE and TTF corresponds to increase in hole and electron doping respectively.

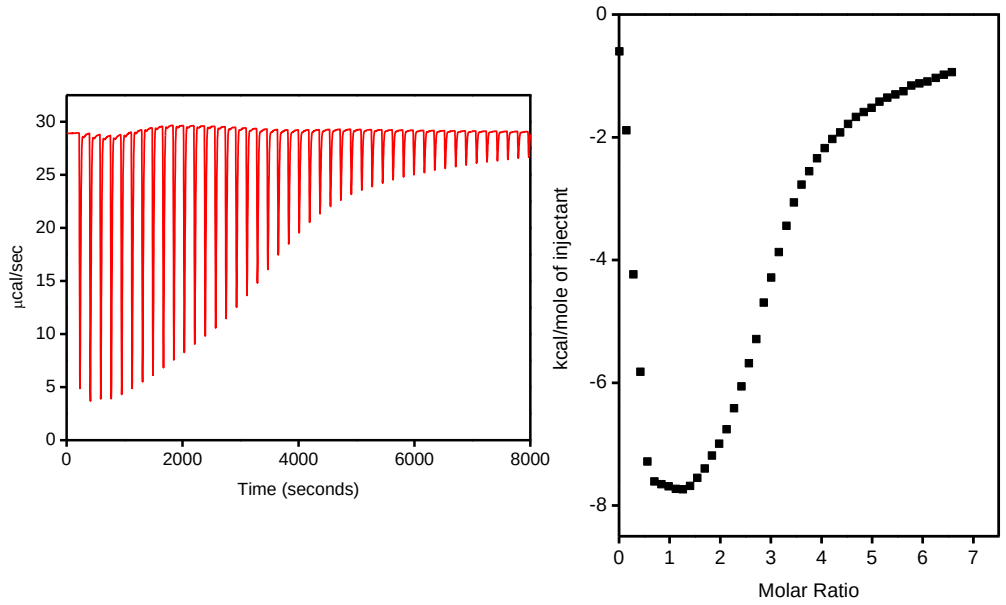

Figure 4: (a) Raw ITC data for titration of TCNE vs. Phosphorene (b) Integrated heat response plot

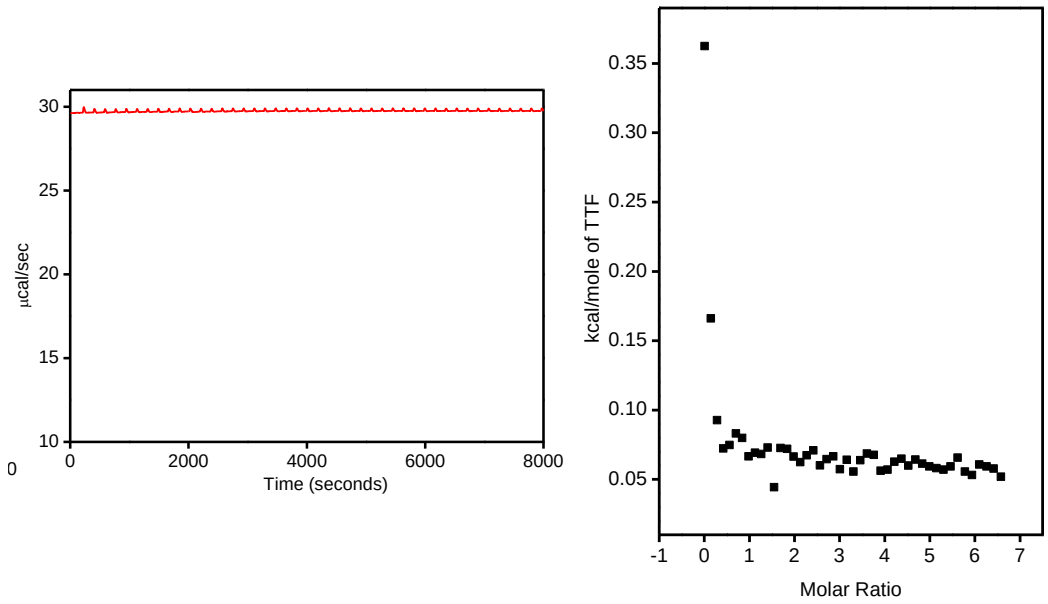

Figure 5: (a) Raw ITC data for titration of TTF vs. Phosphorene (b) Integrated heat response plot

Figures 4 and 5 show the ITC plots for TCNE and TTF respectively. The interaction energies (integrated heat at first injection) calculated for TCNE is -7.95 kcalmol^{-1}. TTF does not interact strongly and we are unable to measure any sizeable heat of reaction. Thus TCNE interacts more strongly than TTF, as suggested by Raman data.

First-principles calculations carried out by Arkamita Bandyopadhyay and Prof. Swapan K. Pati, show that TCNE and TTF molecules lay flat on the phosphorene at distances of 3.32 and

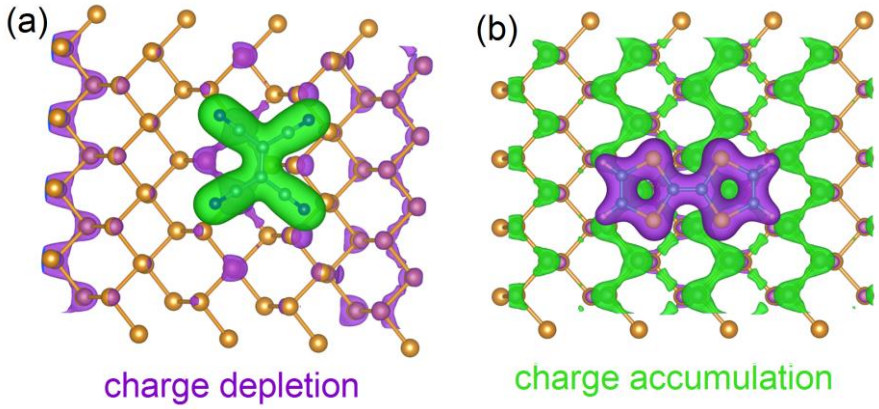

Figure 6: Charge density maps of phosphorene with (a) TCNE and (b) TTF, calculated by first principles calculations

3.15 Å respectively. Charge-transfer in the case of TCNE is 0.346e while in the case of TTF it is 0.187e. Thus, TCNE as an acceptor interacts more strongly through charge transfer. Interestingly, the distance of the central C=C bond in TCNE deceases from 1.43 Å to 1.40 Å because of its electron accepting character. The C=C bond of the donor TTF, on the other hand, increases from 1.35 Å to 1.37 Å. Charge difference maps reveal the nature of charge transfer between phosphorene and the interacting molecules. In **Figure** 6, we show the charge density difference maps depicting the interaction between phosphorene and TCNE and TTF respectively. The green lobes represent charge accumulation and the purple lobes depict charge depletion.

Charge transfer interaction with aromatic donors and acceptors

Our study of the interaction of phosphorene with aromatic donors and acceptors has yielded interesting results. In **Figure** 7, we see the effect of the donor D2 and the acceptor A2 on the Raman spectrum of phosphorene. These molecules also cause

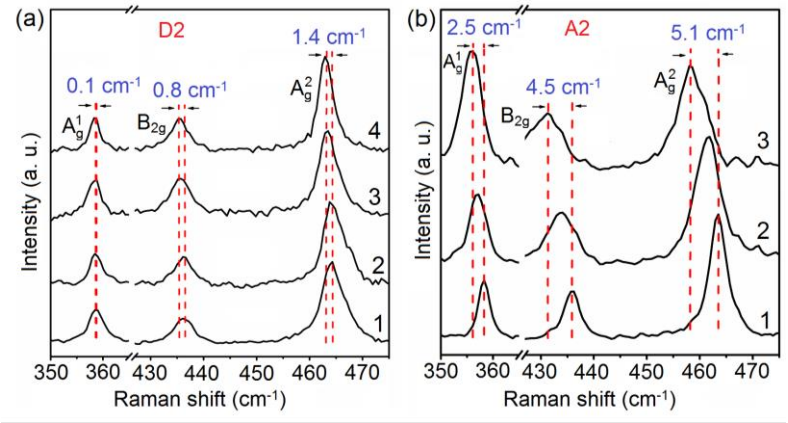

Figure 7: Raman bands of phosphorene on interaction with varying concentrations of (a) electron donor D2 (**1**; 0.0, **2**; 0.5, **3**; 0.8 and **4**; 1.0 mM) and (b) electron acceptor A2 (**1**; 0.0, **2**; 0.5 and **3**; 1.0 μM).

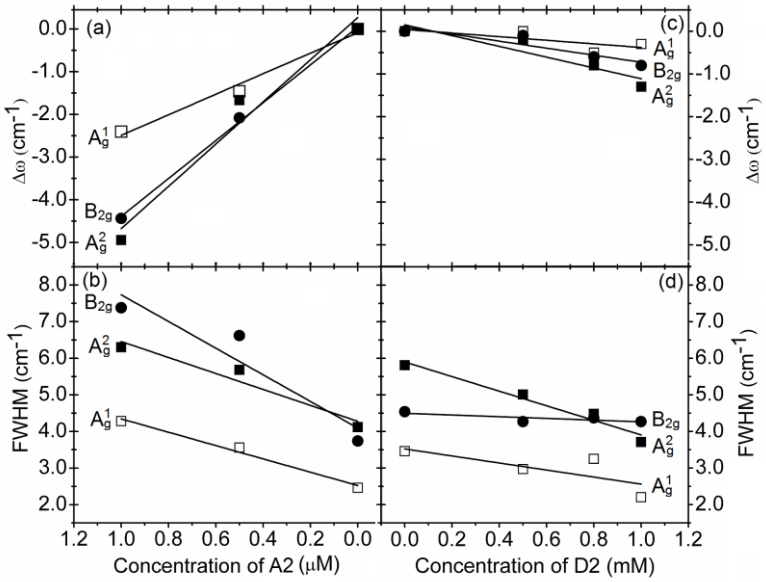

Figure 8: Shifts of the phonon frequencies (Δω) and the full width at half maxima (FWHM) of A_g^1, B_{2g} and A_g^2 bands of phosphorene as the function of concentration of (a-b) A2 and (c-d) D2. Increase in concentration of A2 and D2 corresponds to increase in hole and electron doping respectively.

softening of the Raman bands along with the broadening of the bands (**Figure** 8). In fact the frequency shifts of all the three bands due to the donor D2 are comparable, and also small as compared to the shifts caused by the acceptor A2. However the effects of acceptor are significant causing much larger frequency shift as well as broadening.

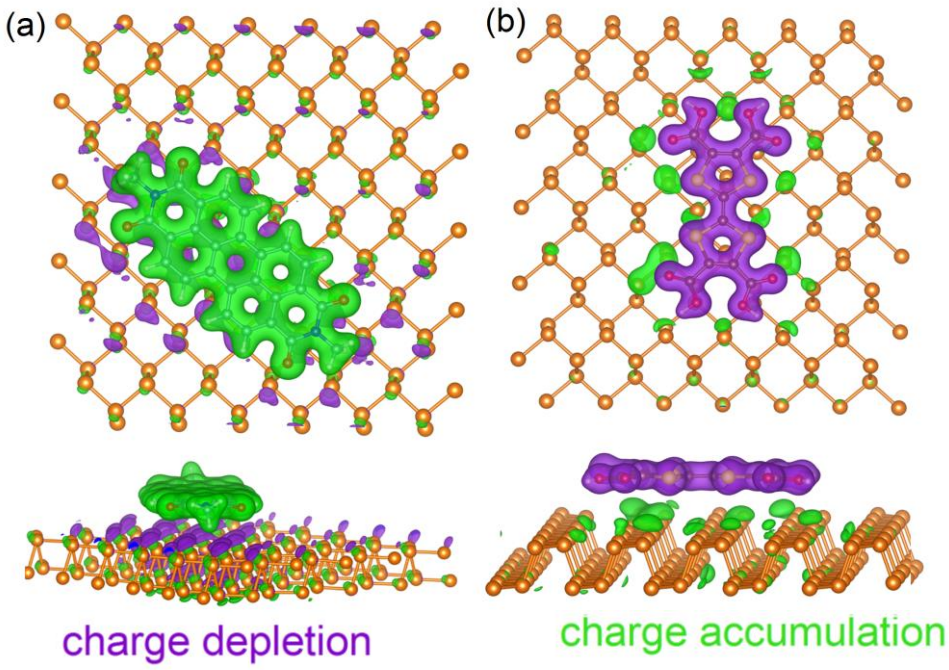

Figure 9: Charge density maps of phosphorene with (a) A2 and (b) D2, calculated by first principles calculations

First-principles calculations carried out by Arkamita Bandyopadhyay and Prof. Swapan K. Pati, in the case of aromatic acceptor A2 shows large charge-transfer (0.17e) compared to the donor D2 (0.04e). The distance between A2 and phosphorene is 3.33 Å and that between D2 and phosphorene is 3.32 Å. Charge difference maps reveal the nature of charge transfer interaction between phosphorene and the donors as well acceptor molecules. **Figure** 9 shows the charge density maps of phosphorene with A2 and D2 respectively. **Figure** 10 shows the density of states (DOS) for D2 and A2. D2 shows a donor level just below the Fermi energy, while for A2, a molecular acceptor level arises. This confirms the occurrence of charge transfer interaction. Acceptors take electrons from the filled p_z orbitals of phosphorus. These electrons are delocalized in nature, whereas donor molecules give electrons to the narrow vacant 3d-bands of phosphorene. Hence for donors, the electrons are donated to the localized

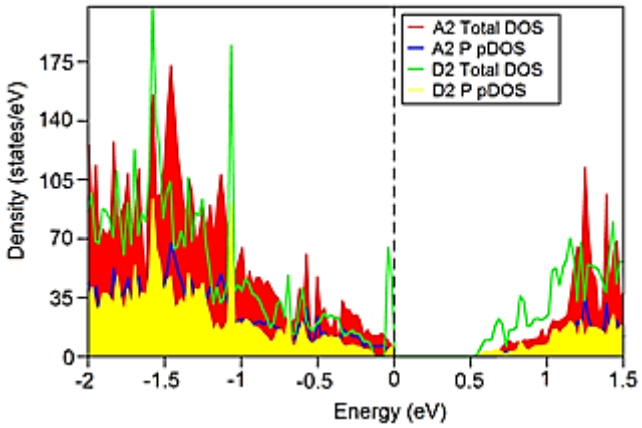

Figure 10: Projected density of states (pDOS) plot for A2 and D2

orbitals, and because of this, the donor molecule-phosphorene interaction becomes unfavourable compared to that of the acceptors.

We have investigated the UV-visible spectra of aromatic donors and acceptors in the presence of phosphorene. In **Figure** 11a, we show the absorption spectra of D2 as a function of concentration of phosphorene. **Figure** 11b shows the absorption spectra of A2 as a function of the concentration of phosphorene. The changes in the band intensities with increasing concentration of phosphorene confirm the interaction of the donor and acceptor molecules with phosphorene. Making use of absorption band intensities, we calculated the association constants (K_a) of D1, D2, A1 and A2 with phosphorene using Benesi-Hildebrand plots (**Figure** 12). The association constants of donors D1 and D2 are 7.2 x 10^2 and 5.6 x 10^2 M^{-1} respectively while those of the acceptors A1 and A2 are 6.5 x 10^3 and 1.9 x 10^3 M^{-1} respectively. Clearly, acceptors interact much strongly than the donors, in accordance with the conclusions from Raman studies.

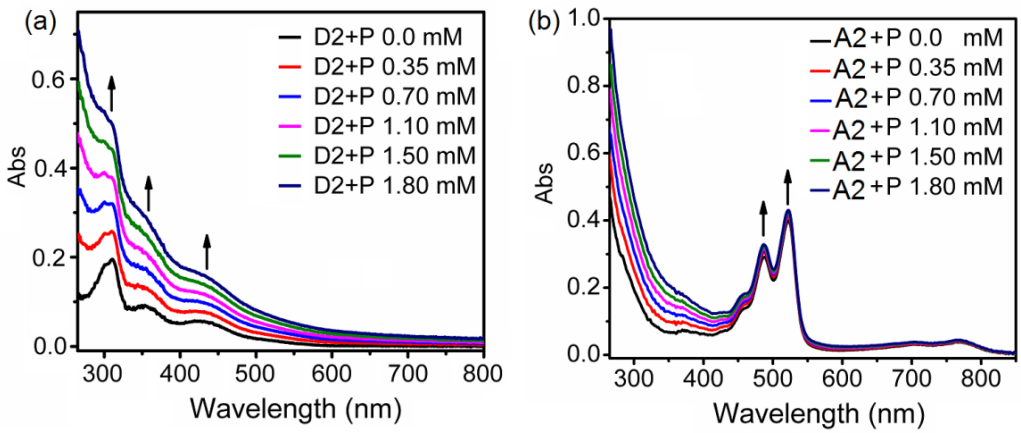

Figure 11: Absorption spectra of (a) D2 and (b) A2 with increasing concentration of phosphorene

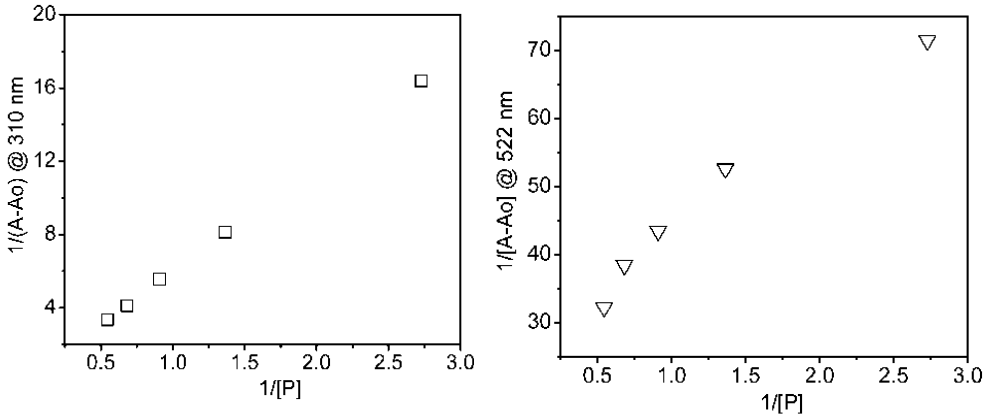

Figure 12: Benesi-Hildebrand plots of (a) D2 and (b) A2 with increasing concentration of phosphorene

Phosphorene Quantum dots (PQDs)

Material Characterization

PQDs were prepared from BP by liquid exfoliation in NMP/DMF (**Scheme** 2). The particle size and crystallinity of the PQDs were established by TEM (**Figure**s 13a and 13b). The insets of **Figure** 13 show lattice fringes in the high-resolution TEM images of PQDs. The crystalline nature of the PQDs suggests that the puckered structure is maintained (**Scheme** 2). **Figure**s 13c and 13d show AFM images of PQDs prepared at 187.6 and 225 W power. We see that increasing power of the ultrasonic waves leads to a decrease in the particle size. The average diameter of particles prepared at 150, 187.5 and 225 W power is 5.0, 3.5 and 1.0 nm

respectively. At 225 W power, there were more particles below 2.0 nm size, some of them reflecting features of monolayers.

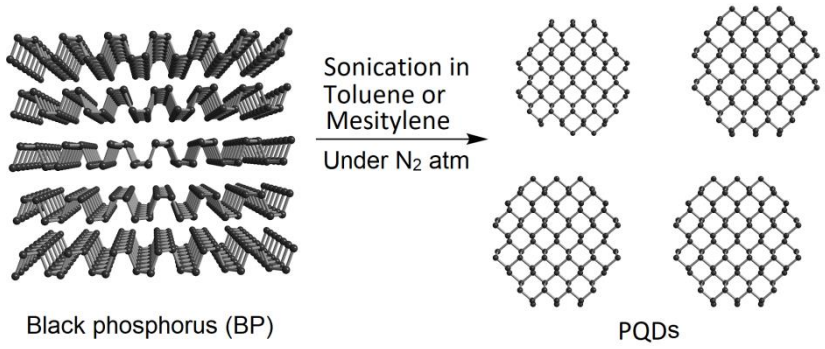

Scheme 2: Schematic representation of preparation of PQDs by liquid exfoliation

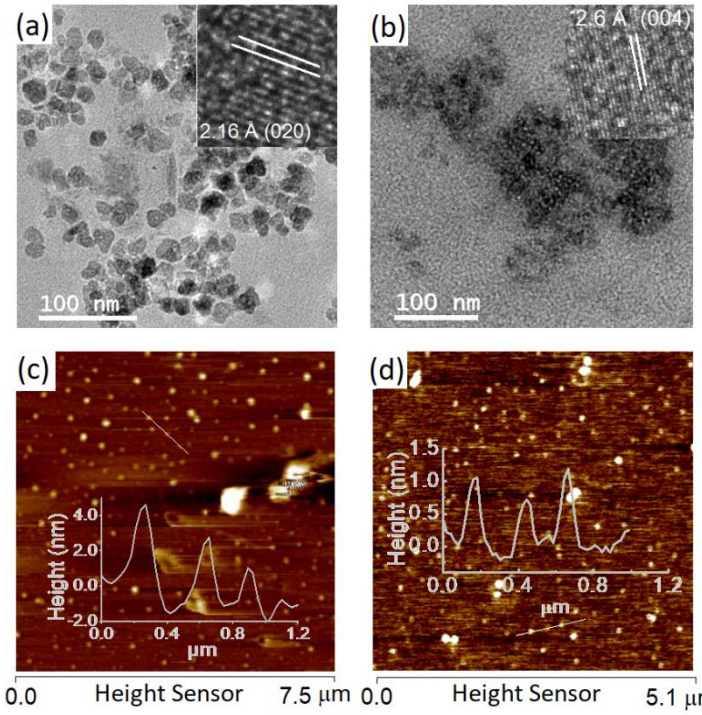

Figure 13: (a-b) TEM images of PQDs (c-d) AFM images of PQDs along with respective height profiles

Figure 14 shows photographs of the PQD dispersion under visible and ultra-violet radiation (365 nm), revealing intense blue emission. The color intensity slightly increases with sonication power from 150 to 225 W. The color intensity under visible and UV radiation remains unchanged after vacuum evaporation of the solvent.

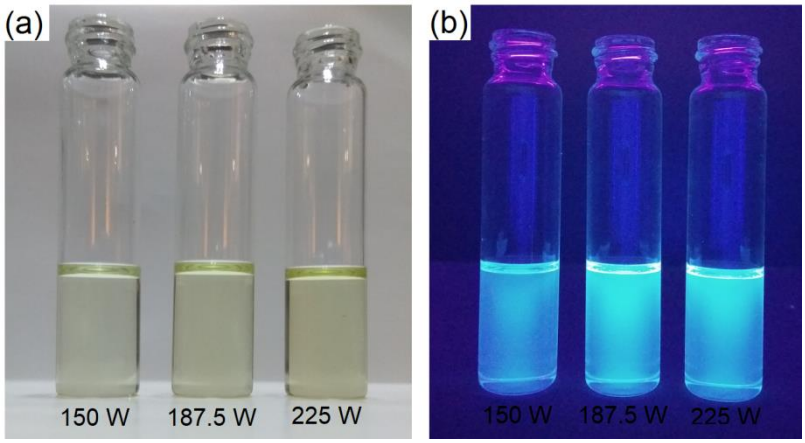

Figure 14: Photographs of the PQD dispersion under visible and ultra-violet radiation (365 nm)

Quenching of the photoluminescence of the PQDs by organic donor and acceptor molecules was examined. It has been reported that tetracyanoethylene (TCNE), tetracyanoquinodimethane (TCNQ) and tetrathiafulvalene (TTF) interact with phosphorene through charge-transfer interaction. All these molecules quench the photoluminescence progressively with increasing their concentration (**Figure** 15a-c). **Figure** 15d shows the Stern-Volmer curves of TTF, TCNE and TCNQ. From the slopes of the linear curves, the Stern-Volmer constants (K_{sv}) are found to be 6.6×10^3, 1.0×10^4 and 7.0×10^4 M^{-1} for TTF, TCNE and TCNQ respectively. The effect of TCNE and TCNQ on the photoluminescence of PQDs is more marked than that of TTF, suggesting that the acceptor binds more efficiently with the phosphorene. In addition, TCNE and TCNQ cause a red-shift, while TTF causes a slight blue-shift of the photoluminescence band.

First principles calculations

First-principles calculations carried out by Madhulika Mazumdar and Prof. Swapan K. Pati, suggest that the PQDs show absorption maxima in the 300-650 nm region of the electromagnetic spectrum. A red-shift is observed in the absorption wavelength (λ_{max}), on

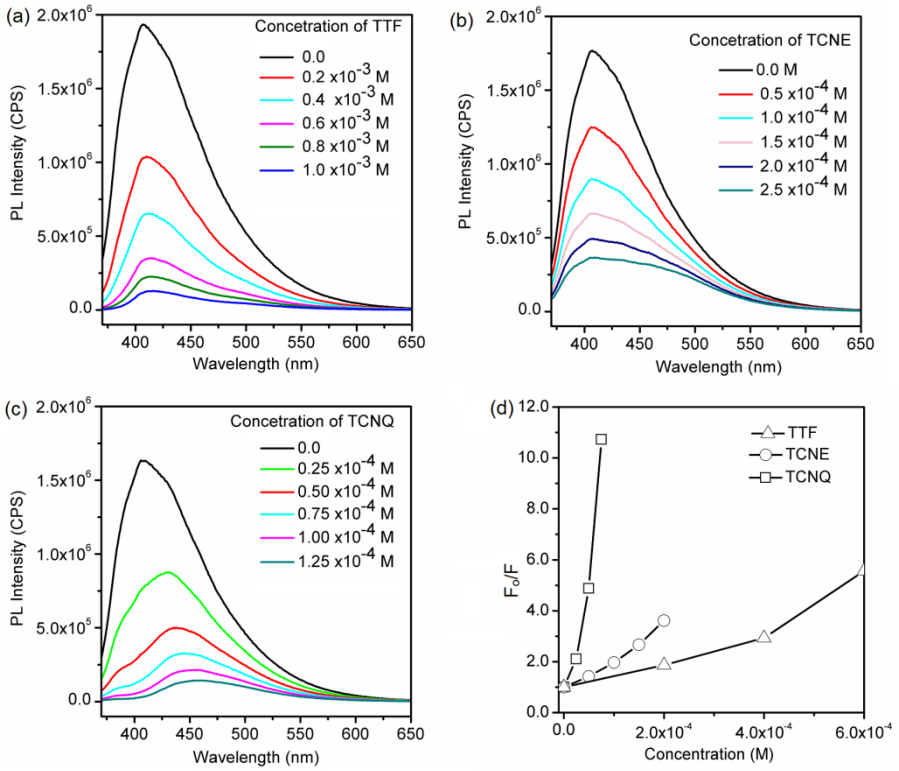

Figure 15: (a-c) Quenching of PL intensity with TTF, TCNE and TCNQ respectively (d) Stern-Volmer plots of TTF, TCNE and TCNQ

wavelength can be attributed to quantum confinement, which creates discretely spaced energy levels. This trend does not follow a smooth function, as the surface and edge structures of PQD do not scale with size. Moreover, the intensities of absorption peaks depend crucially on the surface to bulk ratio of atoms. It increases with increase in size and saturates eventually as the ratio tends to a negligible value. The experimental spectra correspond to 500 atoms which exhibit negligible shift.

Mulliken Population study is an effective tool for studying partial atomic charges that can offer a qualitative insight into the net charge of the system. A differential population analysis of the orbitals proves that PQDs accept electrons from TTF into the empty 3d bands of phosphorus atoms, and donates electrons to TCNE/TCNQ from the 3p bands of phosphorus, as observed from the rise and fall in electronic charge density of the corresponding orbitals respectively.

3.4 Conclusions

We have been able to establish that both holes and electrons can be doped into phosphorene by molecular charge-transfer. Although electron acceptor or hole doping causes a marginally greater effect on the spectral characteristics and magnitude of association, there is no gross electron-hole asymmetry from our Raman and ITC analysis. The present study also demonstrates that stable phosphorene quantum dots with average sizes varying between 1.0 to 5.0 nm can be conveniently prepared by sonication of black phosphorus. The particles size of PQDs can be changed by changing sonication input power. The PQDs exhibit quantum yield in the range of 7.60-9.73%. Electron donors (TTF) as well acceptors (TCNE and TCNQ) quench the photoluminescence, however quenching is more marked with acceptors. Experimentally and theoretically, we observed that both electron donors and acceptors cause red-shift to the absorption spectra.

REFERENCES

1. C.N.R. Rao, U. V. W., *2D inorganic materials beyond graphene*. 1st Ed ed.; World Scientific: Singapore, 2017.
2. H. Liu, A. T. N., Z. Zhu, Z. Luo, X. Xu, D. Tománek and P. D. Ye, *ACS Nano* **2014,** 8.
3. L. Liang, J. W., W. Lin, B. G. Sumpter, V. Meunier and M. Pan, *Nano Lett.* **2014,** 14.
4. S. Das, M. D., A. Roelofs, *ACS Nano* **2014,** 8.
5. F. Xia, H. W. a. Y. J., *Nature Commun.* **2014,** 5.
6. C. Biswanath, G. S. N., S. Anjali, K. Manabendra, K. Chandan, D. V. S. Muthu, D. Anindya, U. V. Waghmare and A. K. Sood, *2D Materials* **2016,** 3.
7. G. Abellán, V. L., U. Mundloch, M. Marcia, C. Neiss, A. Görling, M. Varela, F. Hauke and A. Hirsch, *Angew. Chem., Int. Ed.* **2016,** 55.
8. J. Yu, T. Q., H. Peng, Z. Zhen and S. Panwen, *Nanotechnology* **2015,** 26.
9. J. Yu, T. Q., H. Peng, Z. Zhen, S. Panwen, *Nanotechnology* **2015,** 26.

10. R. Zhang, B. L. a. J. Y., *J. Phys. Chem. C* **2015,** 119.

11. Y. He, F. X., Z. Shao, J. Zhao and J. Jie, *J. Phys. Chem. Lett.* **2015,** 6.

12. S.-T. Han, L. H., X. Wang, Y. Zhou, Y.-J. Zeng, S. Ruan, C. Pan, Z. Peng, *Adv. Sci* **2017,** 4.

13. Z. Sun, H. X., S. Tang, X.-F. Yu, Z. Guo, J. Shao, H. Zhang, H. Huang, H. Wang, P. K. Chu, *Angew. Chem. Int. Ed.* **2015,** 54.

14. S. Ge, L. Z., P. Wang, Y. Fang, *Sci. Rep.* **2016,** 6.

15. W. Gu, X. P., Y. Cheng, C. Zhang, J. Zhang, Y. Yan, C. Ding, Y. Xian, *ACS Sensors* **2017,** 2.

16. J. P. Perdew, K. B. a. M. E., *Phys. Rev. Lett.* **1996,** 77.

17. Joubert, G. K. a. D., *Phys. Rev. B* **1999,** 59.

18. Blöchl, P. E., *Phys. Rev. B* **1994,** 50.

19. J. M. Soler, E. A., J. D. Gale, A. García, J. Jun-quera, P. Ordejón, D.; Sànchez-Portal, *J. Phys. Condens. Matter* **2002,** 14.

20. Frisch, M. J., *Gaussian 09, Revision C.01*. Gaussian, Inc., Wallingford CT: 2010.

21. D. J. Late, A. G., B. Chakraborty, A. K. Sood, U. V. Waghmare and C. N. R. Rao *J. Exp. Nanosci.* **2011,** 6.

22. Voggu, C. N. R. R. a. R., *Materials Today* **2010,** 13.

CHAPTER 4

Covalent functionalization of nanoparticles of semiconducting metal chalcogenides*

SUMMARY

Covalent functionalization of semiconducting chalcogenide nanoparticles ZnS, CdS and ZnSe by reaction with organic halides has been demonstrated. Functionalized chalcogenides exibit a charge-transfer band at higher wavelengths, a claim supported by DFT calculations.

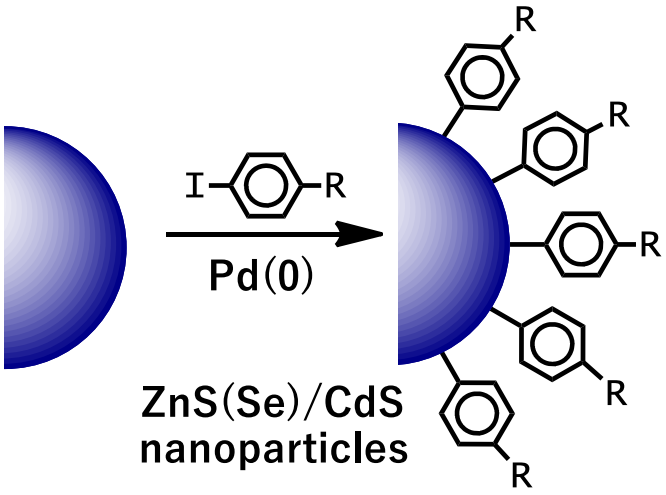

**A paper related to this work has appeared in Chem Nano Mat (2018)*

4.1 Introduction

Chemical modification of nanomaterials by functional groups has become an active area of research in recent years. Functionalization enables us to tune the physical and chemical properties of the material of interest according to our requirements[1-5]. Solubility and dispersability in different solvents can also be affected by surface modification. Recently there have been reports on covalent functionalization of metallic 1T MoS_2 using organic halides[2]. The nucleophilic reaction occurs because of electron transfer between the metallic 1T phase and the halide, resulting in forming the covalent C—S bond. Interestingly, semiconducting sheets of the stable 2H MoS_2 have been functionalized by reaction with iodobenzenes in the presence of a Pd(0) catalyst[6, 7]. It has also been shown that other organic bromides and iodides including certain fluorophores react with the MoS_2 sheets forming C—S bonds. Encouraged by these results, we have employed a similar concept to functionalize semiconducting metal chalcogenide nanoparticles such as ZnS, CdS and ZnSe. Covalent functionalization results charge-transfer between the sulphide and the benzene, which is shown by a band in the absorption spectra at the higher wavelength region. DFT calculations carried out to understand the electronic structure and properties of the functionalized nanoparticles, predict the occurrence of the charge-transfer band.

4.2 Experimental

Materials

Zinc acetate, $Zn(OAc)_2 \cdot 2H_2O$ (SDFCL, India), $Cd(OAc)_2.2H_2O$ (Merck, India) and $Na_2S.9H_2O$ (SDFCL, India), selenourea (Alfa-Aesar), iodobenzene (Spectrochem, India), 4-nitroiodobenzene (TCI, Japan), and 4-iodoanisole (Sigma-Aldrich, India), 1-

(bromoacetyl)pyrene (Sigma-Aldrich, India), 3-acetyl-6-bromocoumarin (TCI, Japan), toluene (Spectrochem, India) and N,N′-dimethylformamide (Spectrochem, India) were purchased from commercial sources and used as received. Absolute ethanol was purchased from Hymen, UK. DI water was used in the synthesis.

Synthesis

Synthesis of ZnS, CdS and CdSe nanoparticles

For the synthesis of ZnS nanoparticles[8], Zinc acetate (1 g, 5 mmol) was dissolved in 200 mL water. The solution was then stirred at room temperature till it dissolves. Into it Sodium sulphide (1.8 g, 7 mmol) dissolved in 100 mL water was slowly added. The solution was further stirred for 20 minute during which it turns white. This solution was then centrifuged and the solid obtained was further washed several times with water. The solid product was then dried under vacuum at 60 °C. CdS nanoparticles were synthesized in a similar manner, by using Cadmium acetate (1.33 g, 5 mmol) in place of Zinc acetate. CdS nanoparticles obtained were orange in colour.

For the synthesis of ZnSe nanoparticles[9], Zinc acetate (450 mg, 2.25 mmol) and Seleno urea (240 mg, 1.95 mmol) were dissolved in 70 mL of water and then sonicated for an hourunder Argon atmosphere. The solution was then centrifuged and the solid obtained was washed several times with water and then ethanol and then finally dried under vacuum. ZnSe nanoparticles synthesized were yellow in colour.

Synthesis of functionalised chalcogenides

All the reactions were carried in out in an inert (nitrogen) atmosphere using standard Schlenk techniques. As-synthesized ZnS nanoparticles iodobenzene, *p*-iodoanisole or *p*-nitrobenzene (amounts as in **Table** 1) and dry toluene (10 mL) were taken in a 50 mL Schlenk flask

containing a magnetic bar. The resulting mixture was frozen in an acetone/liquid nitrogen bath and degassed by three successive freeze-pump-thaw cycles. Tetrakis[triphenylphosphine]palladium(0) ($Pd(PPh_3)_4$) (2.5 mol%) was added to the reaction mixture and sonicated for 30 minutes under nitrogen atmosphere. The reaction mixture was refluxed at 110 °C for 24 hours under nitrogen atmosphere while stirring, then allowed to cool to room temperature. The precipitate collected by centrifugation was thoroughly washed with absolute ethanol and dried under vacuum at 60 °C. The reactions of ZnS nanoparticles with 1-(bromoacetyl)pyrene and 3-acetyl-6-bromocoumarin were carried out in a similar way. The reactions of CdS and ZnSe with iodobenzene were carried out in a similar way as ZnS (**Table** 1). Dry N,N-dimethylformamide was used as a solvent in the case of the functionalization of ZnSe nanoparticles.

Characterization

Powder X-ray diffraction patterns were collected using a Bruker D8 Discover diffractometer using Cu-Kα radiation. Fourier transform infrared spectra (FTIR) were recorded in a Bruker FTIR specrometer in KBr mode. Extent of functionalization were determined by thermogravimetric analyses carried out in a nitrogen atmosphere with a Metler Toledo TGA-850 TG analyser at the rate of 3 °C/min. Raman spectra were collected in the backscattering geometry using a 514 nm laser with a Jobin Yvon LabRam HR 800 spectrometer. Photoluminescence spectra were recorded with a Fluorolog-3 spectrophotometer fitted with Horiba Jobin Yvon Xe lamp light source. Particles sizes of the nanoparticles were determined by using a NovaNano SEM 600 (FEI) and JEOL-3010 (JEOL) TEM microscopes. UV-visible diffuse reflectance spectra of the power samples were recorded with a Perkin-Elmer Lambda 750 UV/Vis/NIR spectrophotometer using $BaSO_4$ as a reference. The diffuse reflectance

spectra were converted to absorption spectra by using the Kubelka-Munk function[10, 11]. CP-MAS ^{13}C NMR spectra were recorded with a Bruker 400 MHz NMR spectrometer.

First-principles calculations

For optimization of the systems and to calculate the optical properties, the SIESTA package[12] with PBE/DFT-D[13] was used. We have used a mesh cut off the value of 400 Ry. The structures were optimized until the forces on each atom were 0.04 eV/Å. We have used a k-point mesh of 5×5×1 for structural relaxation and 10×10×1 for the calculations optical property.

4.3 Results and discussion

Materials characterization

For the current study, ZnS, CdS and ZnSe nanoparticles of sizes 5-10 nm were synthesized. **Figure** 1shows the TEM images of the as synthesized ZnS nanoparticles.

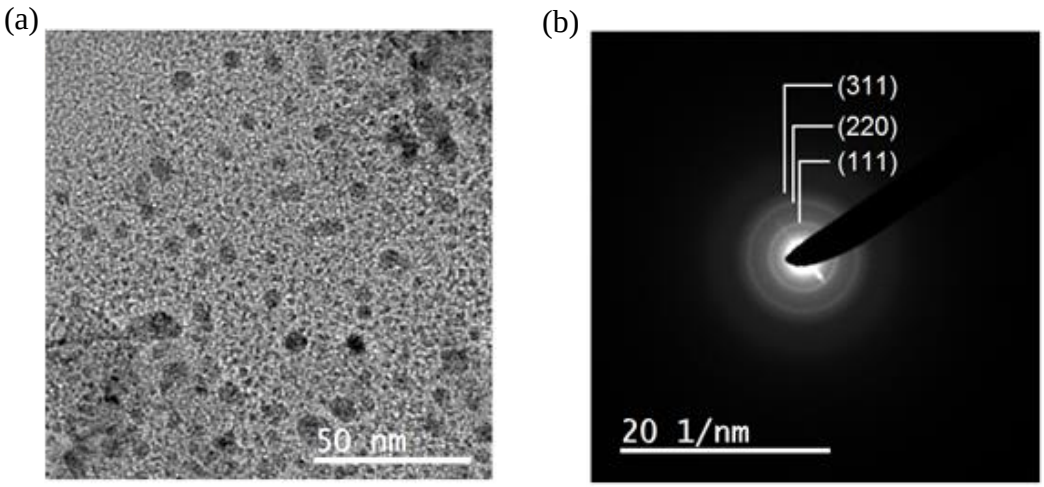

Figure 1: (a) HR-TEM images and (b) SAED pattern of ZnS nanoparticles

ZnS, CdS and ZnSe nanoparticles were covalently functionalized using iodobenzenes. FTIR spectra show the emergence of the C-S and C-Se stretching bands rafter functionalization[1, 2]

(**Figure** 2). We have functionalized ZnS nanoparticles with 4-iodoanisole or 4-iodonitrobenzene using different molar ratios of iodobenzene to study the variation in properties. ZnS work was done with Parvin Fatahi.

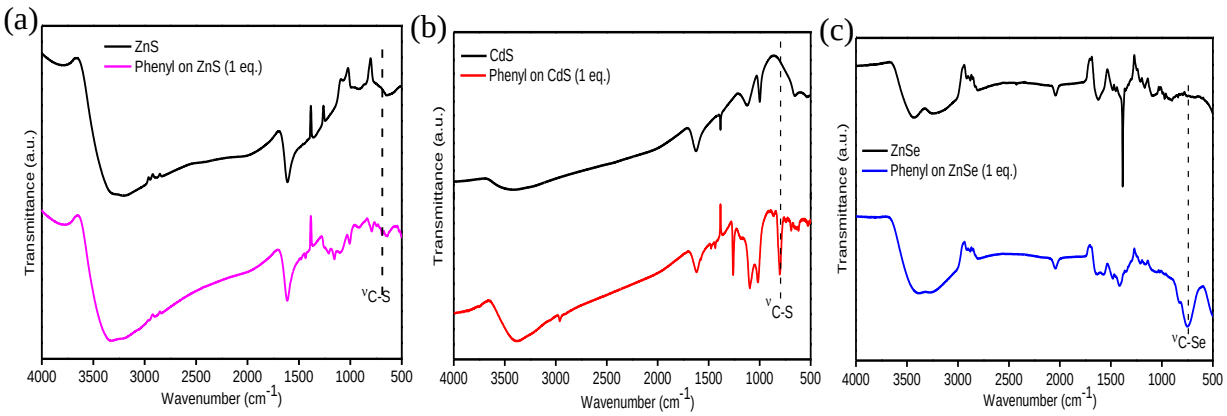

Figure 2: (a-c) FTIR spectra of functionalized nanoparticles of ZnS, CdS and ZnSe respectively

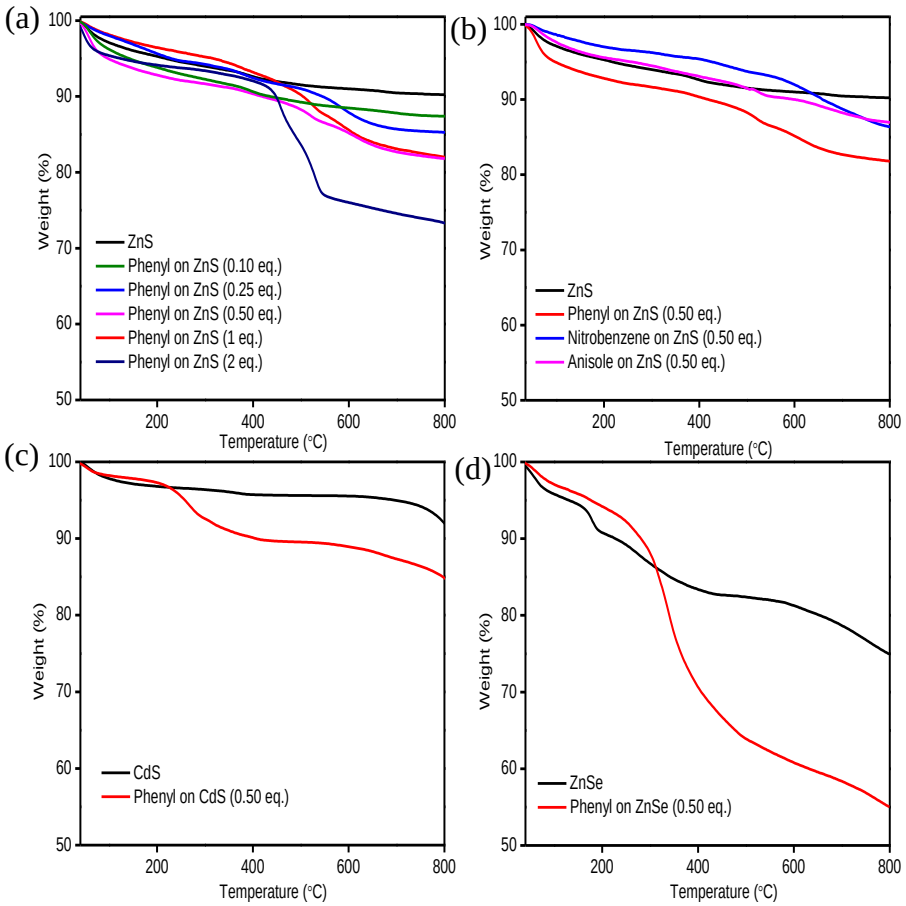

Figure 3: (a) TGA plots of ZnS nanoparticles functionalized with varying amounts of iodobenzene (b) TGA plots of ZnS nanoparticles functionalized with substituted iodobenzenes (c) TGA plot of functionalized CdS nanoparticles (d) TGA plot of functionalized ZnSe nanoparticles

Thermogravimetric analysis shows weight loss due to the loss of the organic residues (**Figure** 3). The weight loss increases with the increase in the ratio of nanoparticle to iodobenzene (**Figure** 3a), exhibiting upto ~ 15% (per S atom) functionalization and also with the substituent on the phenyl ring (**Figure** 3b). The magnitude of functionalization varied with the substituent on the iodobenzene, the electron-withdrawing nitro group favouring functionalization and percentage of functionalization with phenyl and nitrophenyl groups being 5 and 15% per S atom respectively. The presence of the phenyl group on ZnS was confirmed by ^{13}C CP-MAS spectrum (**Figure** 4) and other spectroscopic methods.

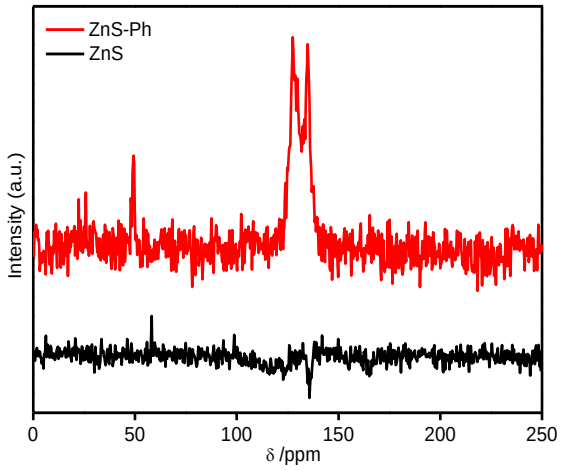

Figure 4: ^{13}C CP-MAS spectrum of ZnS nanoparticles functionalized with phenyl group

The phenyl derivatives of the nanoparticles were coloured, the colour varying with the substituent on the phenyl group. **Figure** 5 shows the picture of ZnS nanoparticles along with its functionalized counterparts. UV-visible absorption spectra of the phenyl functionalized nanoparticles exhibit a long wavelength band in the visible region (**Figure** 6). The absorption maximum shows changes with the substituent on the phenyl group, the nitro group showing a red shift and the methoxy group a blue shift relative to the absorption maximum of the phenyl derivative (**Figure** 6a).

Figure 5: Photographs of (a) ZnS, (b) phenyl on ZnS (0.50 eq.), (c) p-methoxybenzene on ZnS (0.50 eq.), (d) p-nitrobenzene on ZnS (0.50 eq.), (e) pyrene on ZnS (0.50 eq.) and (f) coumarin on ZnS (0.50 eq.)

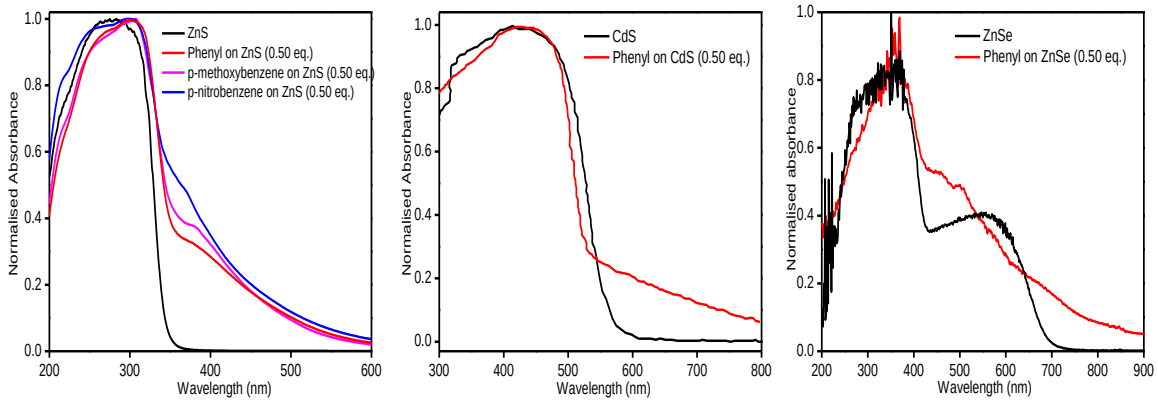

Figure 6: (a) Diffuse reflectance UV-visible spectra of functionalized ZnS nanoparticles. The position of the long wavelength band varies with substituents on phenyl ring (b-c) DRUV-visible spectra of functionalised CdS and ZnSe nanoparticles respectively.

First principles calculations

In order to understand the changes in the electronic structure of the nanoparticles on covalent functionalization and to particularly understand the origin of the long wavelength absorption band, first principles calculations were done by Arkamita Bandyopadhyay and Prof. Swapan K. Pati (**Figure**s 7-9). For **Figure** 7a, we constructed the crystal structure of ZnS nanoparticles by diluting the structure and optimizing the initial structures in each case. We then attached an appropriate number of benzene rings to the surface thiol group and

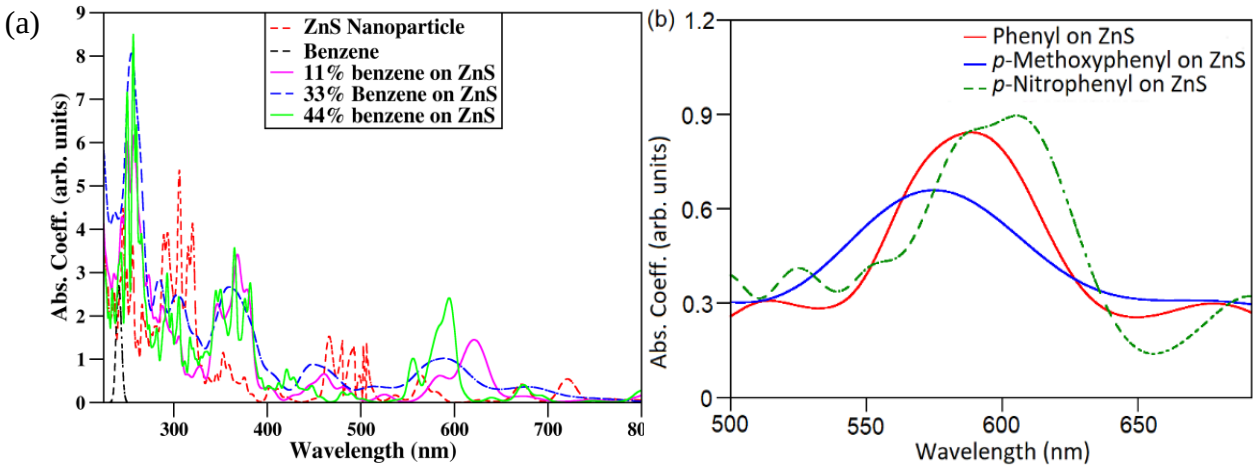

Figure 7: (a) Calculated absorption spectra of functionalized ZnS nanoparticles (b) Charge-transfer bands in functionalized ZnS nanoparticles

optimized the structure again. We varied the benzene concentration on the surface from 11% to 44%, and calculated the opto-electronic properties, particularly the absorption spectra. We

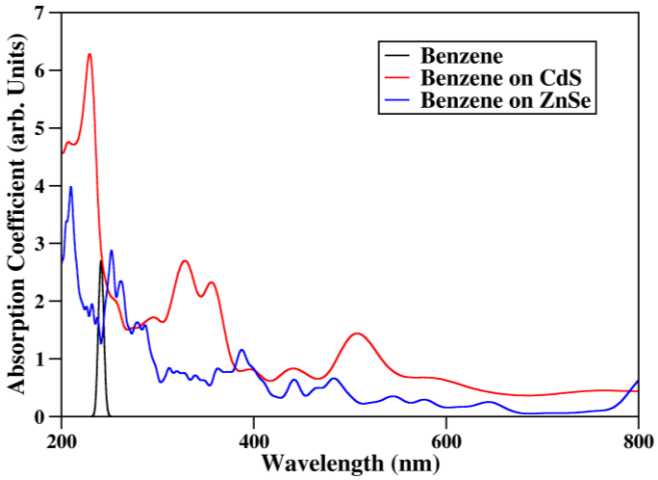

Figure 8: Calculated absorption spectra of functionalized CdS and ZnSe nanoparticles

find that the nature of the transitions remains same in all concentration limits, although for a higher concentration of benzene, there appear a few low energy weak peaks because of benzene to benzene intermolecular π-π transitions. However, the feature corresponding to the surface-benzene interactions remains the same. We find a long wavelength charge-transfer (CT) of 0.36 e from the surface atoms of the nanoparticles to benzene molecules on the

surface, and the CT band appearing at a longer wavelength (580 nm). The difference in the values between calculated and observed CT absorption maxima is due to the limitations inherent to DFT calculations. We also calculated long-wavelength absorption bands with different substituents on benzene (**Figure** 7b). The electron-donating group on benzene blue shifts and electron-withdrawing group on benzene red shifts the CT band, in agreement with the experimental observations. This happens due to the more effective charge-transfer in the presence of the electron withdrawing nitro group. **Figure** 8 shows the calculated absorption spectra of functionalized CdS and ZnSe nanoparticles. First-principles calculations predict

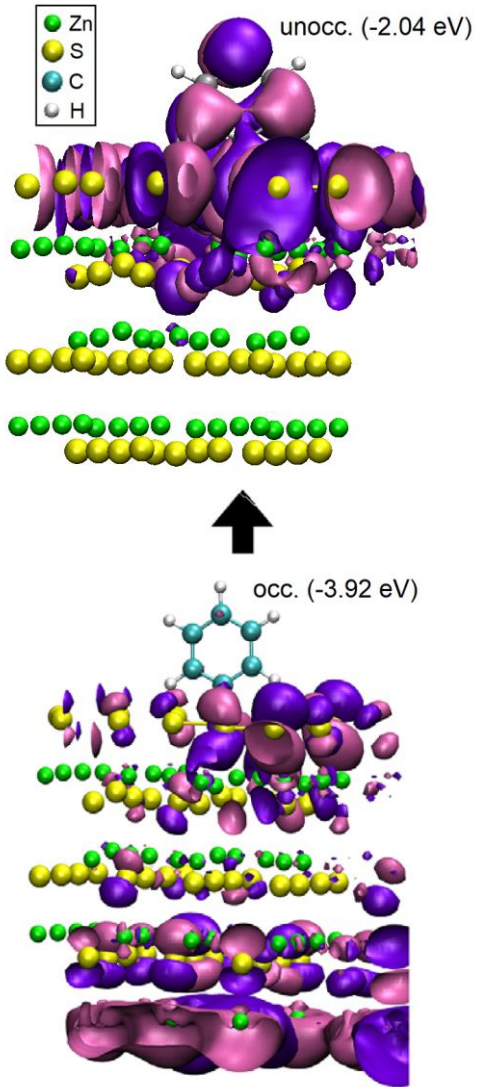

Figure 9: HOMO and LUMO wavefunction plots for the CT band of functionalised ZnS nanoparticles

CT bands at long-wavelengths both in the case of CdS and ZnSe, with absorption maxima around 500 and 800 nm respectively. The nature of CT interactions is similar in all the chalcogenides as they occur between the p orbitals of benzene and 2p and 3p orbitals of surface S or Se atoms. **Figure** 9 shows the HOMO and LUMO wavefunction plots for the CT band of functionalised ZnS nanoparticles. It clearly shows that the absorption is due to charge transfer between the ZnS nanoparticle and the benzene ring.

Functionalization of chalcogenide nanoparticles with fluorescent dyes

We have covalently functionalized ZnS nanoparticles with 1-(bromoacetyl)pyrene and 3-acetyl-6-bromocoumarin dyes. Thermogravimetric analysis indicated 3 and 5% per S atom functionalization respectively with the pyrene and coumarin. The UV-vis absorption and photoluminescence spectra of the functionalized ZnS nanoparticles exhibit changes including marked red-shifts compared to the pristine dye (**Figure** 10).

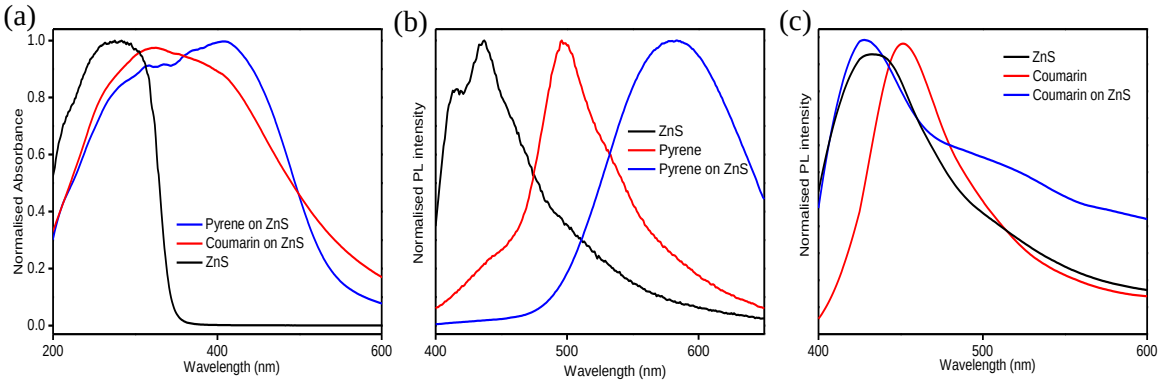

Figure 10: (a) Diffuse reflectance UV-visible spectra of ZnS nanoparticles functionalized with pyrene and coumarin dyes along with pristine ZnS (b) PL spectra of Pyrene functionalized ZnS (c) PL spectra of coumarin functionalized ZnS

We have conducted photoluminescence titration of a mixture of the donor 2-(bromoacetyl)naphthalene and the acceptor 3-(bromoacetyl)coumarin with increasing

concentration of ZnS[14, 15] (**Figure** 11). The photoluminescence spectrum of 2-(bromoacetyl)naphthalene on excitation at 280 nm shows an emission band around 340 nm. The mixture upon addition of ZnS gives rise to a broad coumarin based emission band around 420 nm. The decrease in the intensity of naphthalene based emission band and increase in the coumarin based band indicates Förster resonance energy transfer (FRET) between the donor and the acceptor.

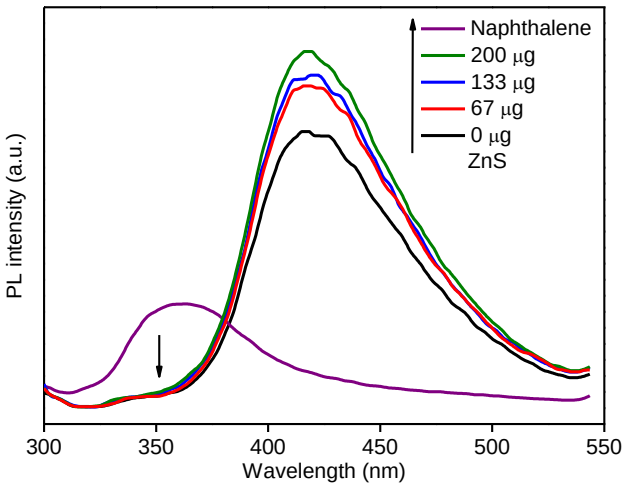

Figure 11: Fluorescence emission spectra of the mixture of naphthalene and coumarin in the presence of increasing concentration of ZnS

4.4 Conclusions

In conclusion, we are able to covalently functionalize nanoparticles of ZnS, CdS and ZnSe with iodobenzenes and other organic halides. This is a noteworthy finding and it would be rewarding to investigate optical and other properties of these materials, some of which may have practical implications. The current results prompt us to believe that it would be possible to attach multi-chromophoric donor-acceptor dyads (such as naphthalene-coumarin) to the surface of semiconducting metal chalcogenide nanoparticles to examine Förster resonance energy transfer (FRET).

REFERENCES

1. B. Pelaz, P. d. P., P. Maffre, R. Hartmann, M. Gallego, S. Rivera-Fernán- dez, J. M. de la Fuente, G. U. Nienhaus, W. J. Parak, *ACS Nano* **2015,** 9.

2. D. Voiry, A. G., R. Kappera, C. de Carvalho Castro e Silva, D. Kaplan, T. Fujita, M. Chen, T. Asefa, M. Chhowalla, *Nat. Chem.* **2015,** 7.

3. R. N. Grass, E. K. A., W. J. Stark, *Angew. Chem. Int. Ed.* **2007,** 46.

4. S. Presolski, M. P., *Mater. Today* **2016,** 19.

5. U. Maitra, A. J., S. J. George, C. N. R. Rao, *Nanoscale* **2011,** 3.

6. P. Vishnoi, A. S., U. V. Waghmare, C. N. R. Rao, *Chem. Eur. J.* **2017,** 23.

7. S. Manjunatha, S. R., P. Vishnoi, C. N. R. Rao, *J. Mater. Res.* **2017**.

8. K. Hongo, H. S., *J. Appl. Phys* **1997,** 82.

9. J. Zhu, Y. K., A. Gedanken, *Chem. Mater.* **2000,** 12.

10. P. Kubelka, F. M., *Tech. Phys.* **1931,** 12.

11. W. W. Wendlandt, H. G. H., *Reflectance Spectroscopy*. Interscience Publishers, New York: 1966.

12. J. M. Soler, E. A., J. D. Gale, A. Garc&a, J. Jun-quera, P. Ordejjn, D. Sanchez-Portal, *J. Phys. Condens. Matter* **2002,** 14.

13. Grimme, S., *J. Comput. Chem.* **2006,** 27.

14. M. Suresh, A. K. M., E. Suresh, A. Das, *Chem. Sci.* **2013,** 4.

15. M. Zuffo, F. D., V. Spalluto, S. Ladame, M. Freccero, *Chem. Eur. J.* **2015,** 21.

CHAPTER 5

Pure germanane

SUMMARY

We have synthesized pure germanane (Ge-H) from $CaGe_2$ by the room temperature reaction with different acids. Investigations on substitution of the Ge-H bond in germananes have been initiated.

5.1 Introduction

In recent years, germanene, a 2D analogue of graphene has garnered attention[1-3]. It has been possible to chemically synthesize germanane (hydrogenated germanene) from the Zintle phase $CaGe_2$ by treatment with HCl at -40 °C[4]. Germanane is expected to have promising electronic and optical properties[5]. The electron mobility, limited by electron-phonon scattering, has been calculated to be around 20 000 cm^2Vs^{-1} at room temperature[6]. There have also been reports on covalent modification of germanane which in-turn affects its properties like band-gap, fluorescence quantum yield and thermal stability[7].

In the literature report on synthesis of germanane by reaction of $CaGe_2$ with HCl at -40°C , product contained little Cl suggesting that the product was not pure. Our aim was to synthesize pure germanane. We have synthesized germanane from $CaGe_2$ by treatment with seven different acids at room temperature. The acids used are H_3PO_4, H_2SO_4, HNO_3, HF, and and CH_3COOH, besides HCl. One of the main objectives of the study was to obtain pure germanane by use of acids other than HCl.

5.2 Experimental

Materials

Granular Calcium (Sigma-Aldrich), Germanium metal powder (Sigma-Aldrich), Iodine monochloride (Sigma-Aldrich) were purchased from commercial sources and were used without further purification.

Synthesis

Synthesis of Calcium Germanide ($CaGe_2$)

Calcium germanide was synthesized as reported elsewhere. Typically, stoichiometric

amounts of Ca and Ge were sealed into a quartz tube under 10^{-6} millibar vacuum. The mixture was annealed at 1025 °C for 20 hours followed by slow cooling over 5 days upto room temperature. CaGe2 crystals obtained were grey in colour and were of high purity as indicated by XRD analysis.

Synthesis and Germanane by acid treatment

Germanane was synthesized by treatment of $CaGe_2$ crystals with different acids. Typically to 100 mg of $CaGe_2$ taken in centrifuge tubes, 2 mL of concentrated solution of HCl, HF, H_2SO_4, H_3PO_4, HCOOH, CH_3COOH and HNO_3 were added and the solution was stirred at room temperature for 7 days. The solid product was then centrifuged out and washed with methanol and dried.

Reaction of $CaGe_2$ with Iodine monochloride (ICl)

To a Schlenk flask containing 20 mg of $CaGe_2$ under vacuum, 20 mL of degassed acetonitrile was added under N_2 atmosphere. 25 mg of ICl was added into the Schlenk flask. The mixture was sonicated for an hour, followed by room temperature stirring for 24 hours under N_2 atmosphere. Solid product obtained via centrifugation, was then thoroughly washed with acetonitrile and vacuum dried.

Characterization

Powder X-ray diffraction patterns were collected using a Bruker D8 Discover diffractometer using Cu-Kα radiation. Raman spectra were collected in the backscattering geometry using a 632 nm HeNe laser with a Jobin Yvon LabRam HR 800 spectrometer. Fourier transform infrared spectra (FTIR) were recorded in a Bruker FTIR specrometer in KBr mode. TEM images were taken in a JEOL-3010 (JEOL) microscope. FESEM imaging was done in a Nova NanoSEM 600 FESEM.

5.3 Results and discussion

Materials characterization

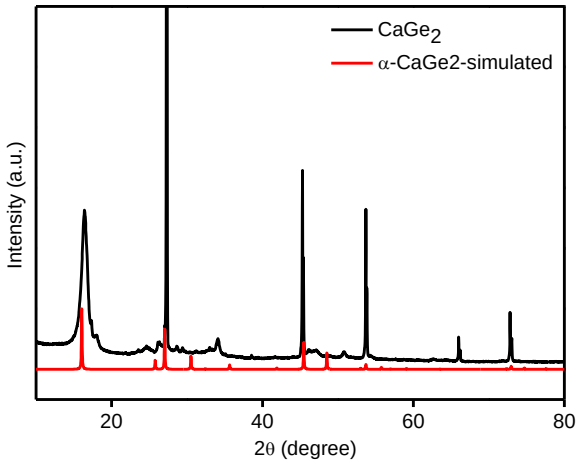

Figure 1: XRD data of synthesized $CaGe_2$ along with simulated α-$CaGe_2$

XRD data confirms the formation of a pure phase α-$CaGe_2$ (**Figure** 1). α-$CaGe_2$ is known to have a hexagonal space group $P6_3mc$ [8]. This structure can be viewed as puckered layers of triply bonded Ge atoms, Ge^{2-}, which is stacked along the direction of the c-axis in ABAB fashion, separated by Ca^{2+} cations. **Figure** 2 shows the XRD plots of $CaGe_2$ treated with the

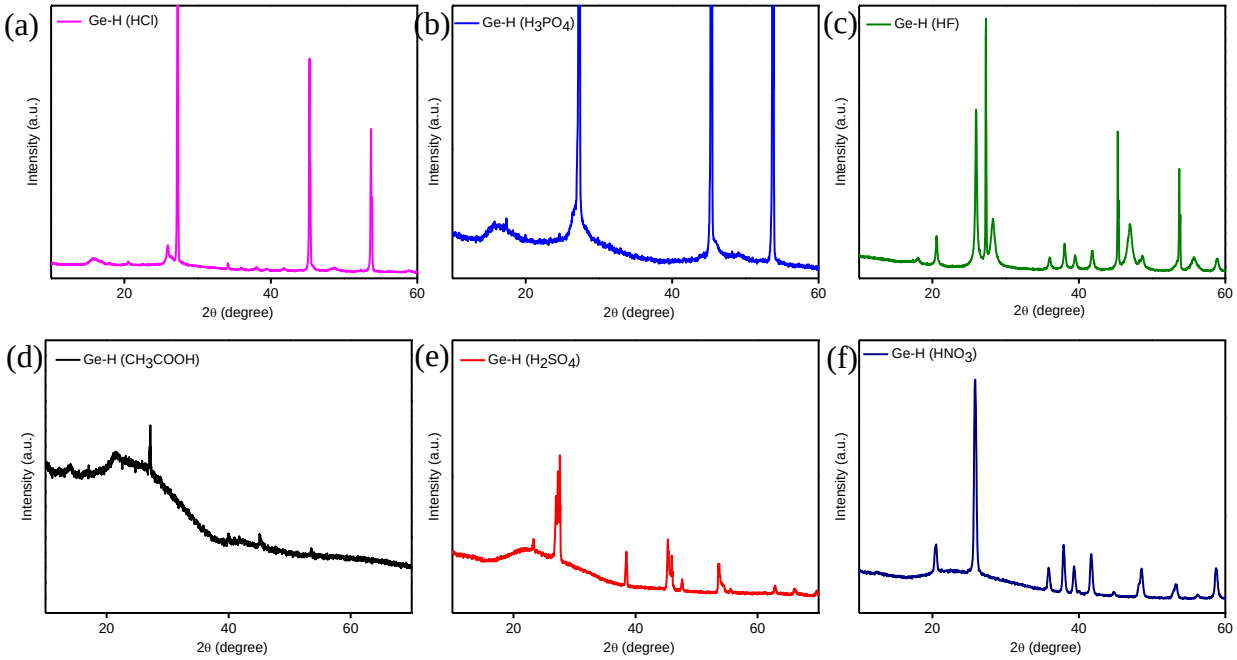

Figure 2: XRD data of Ge-H prepared on treatment with different acids (a) HCl, (b) H_3PO_4, (c) HF, (d) CH_3COOH, (e) H_2SO_4 and (f) HNO_3

different acids.

Acid treatment leads to the formation of pure germanane, Ge-H. XRD of Ge-H obtained from treatment with HCl, H_3PO_4 show that it has the same 2H phase as reported in literature[4]. **Figure** 3 shows the Raman spectra of $CaGe_2$ and germanane prepared from HCl along with bulk germanium metal. From Raman spectra, Ge-Ge stretch for bulk Ge occurs around 307.8 cm^{-1} while for $CaGe_2$ and Ge-H it is slightly blue shifted to 305.7 and 306 cm^{-1} respectively.

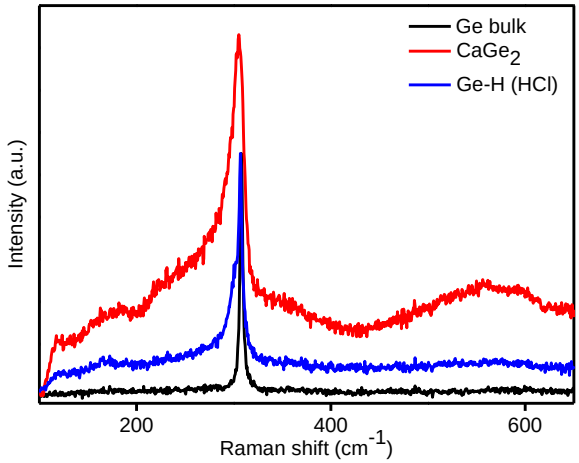

Figure 3: Raman spectra of $CaGe_2$ and Ge-H (HCl) along with Ge bulk

FTIR spectra of germananes give evidence for formation of new Ge-H bond (**Figure** 4). FTIR spectra show Ge-H stretching band around 2000 cm^{-1} and wagging modes at 570, 507 and 475 cm^{-1}. We do not observe the presence of Ge-O-Ge or Ge-O vibrational modes around 800 and 1000 cm^{-1}. The Ge-X bonds (e.g. Ge-Cl) that can be formed on treatment with different acids are not detected in the FTIR spectra as it occurs below 400 cm^{-1}. EDAX of Ge-H (HCl) (**Figure** 5f) however shows presence of trace amounts of Cl atoms.

Figures 5a and b show the FESEM images of $CaGe_2$ and **Figure**s 5c and d shows FESEM images of Ge-H prepared on treatment with HCl and **Figure** 5f shows the corresponding EDAX. **Figures** 5a-d confirms the layered morphology of the synthesized $CaGe_2$ and Ge-H

while EDAX a strong Ge signal, an absence of Ca and O signals, and the presence of trace amounts of Cl. Thus germanane synthesized was highly pure.

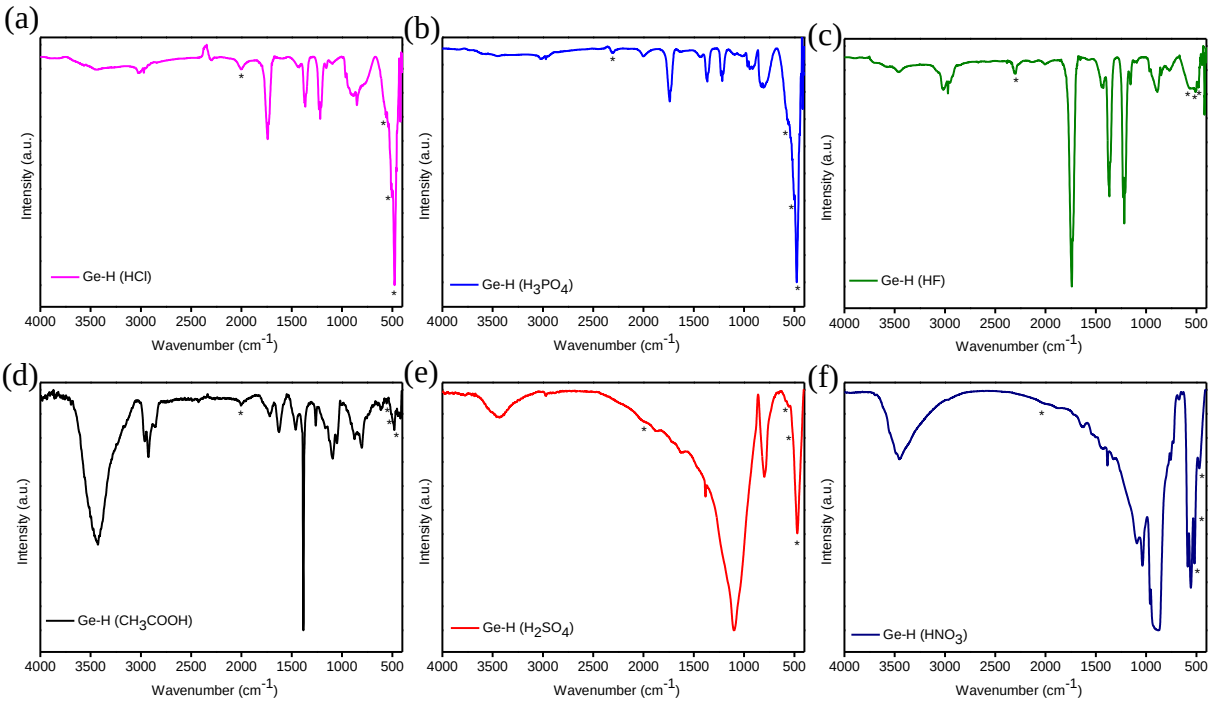

Figure 4: FTIR spectra of Ge-H prepared on treatment with different acids (a) HCl, (b) H_3PO_4, (c) HF, (d) CH_3COOH, (e) H_2SO_4 and (f) HNO_3

Figure 6a shows a TEM image of as synthesized $CaGe_2$ nanosheets and **Figure** 6b shows a TEM image of Ge-H (HCl) while **Figure** 6c shows an electron diffraction pattern for Ge-H showing a hexagonal arrangement of diffraction peaks. It confirms that crystallinity of germanium is maintained on acid treatment.

$CaGe_2$ reactions

We are planning to substitute the Ge-H bond in germananes by reacting it with different reagents. As part of preliminary investigations, we have tried reacting $CaGe_2$ with ICl and characterized the solid product obtained. **Figure** 7 shows the FTIR and Raman spectra of the product obtained. Ge-Ge stretch from Raman spectra for Ge-I is 305.7 cm^{-1}. Further study in

progress.

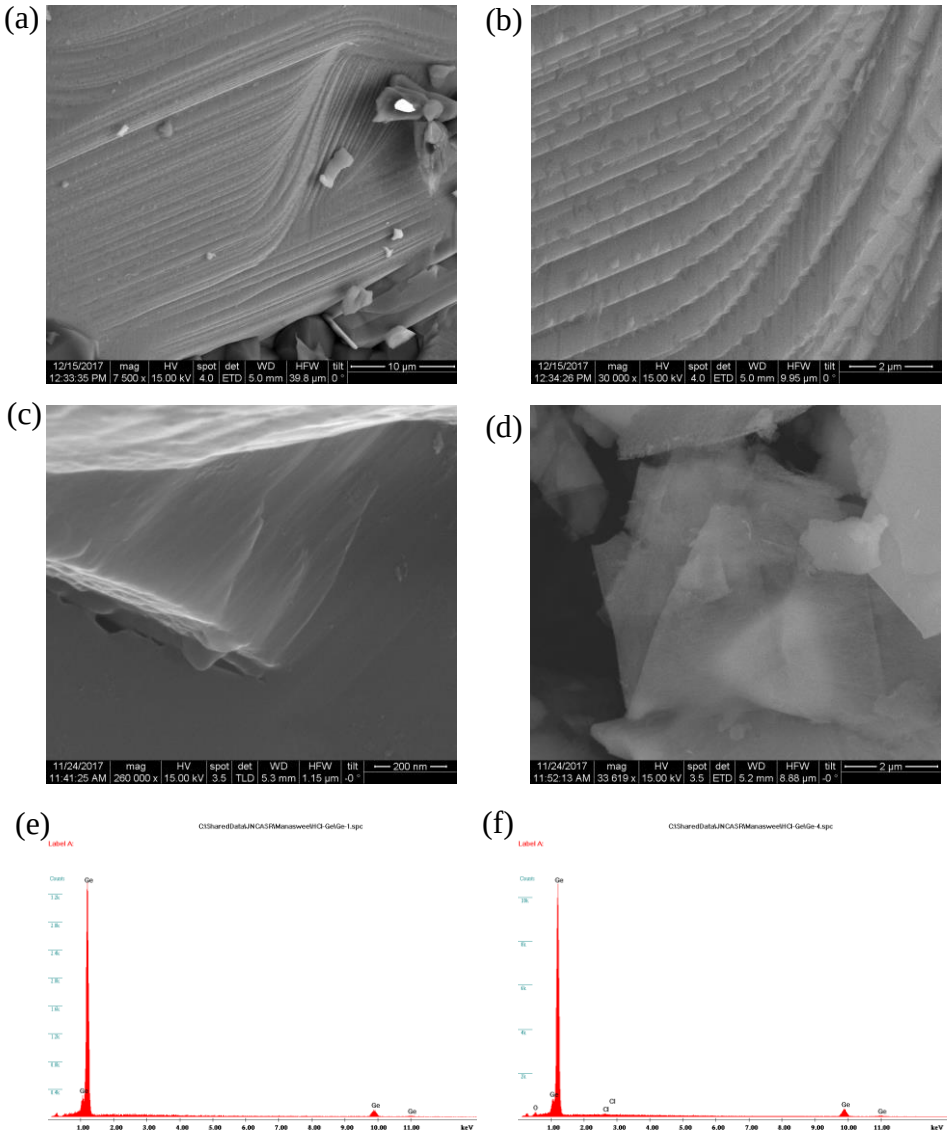

.

Figure 5: (a-b) FESEM images of $CaGe_2$ (b) FESEM images of Ge-H (HCl) (c) EDX of Ge-H (HCl)

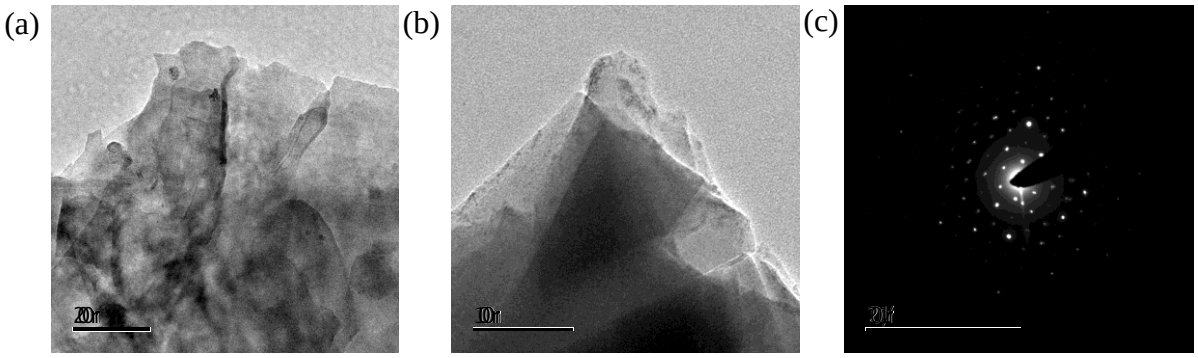

Figure 6: (a) TEM image of $CaGe_2$ (b) TEM image of Ge-H (HCl) (c) ED pattern of Ge-H (HCl)

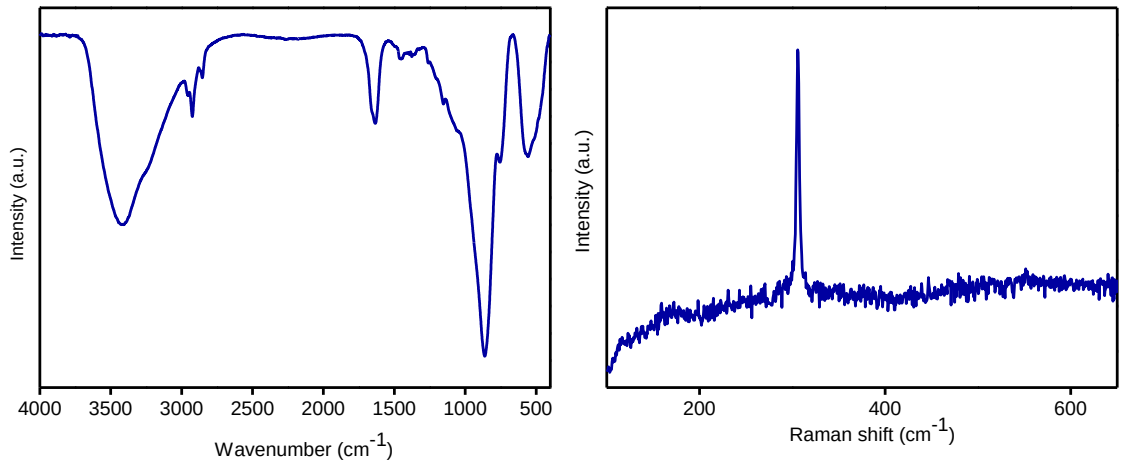

Figure 7: (a) FTIR spectra of Ge-I (b) Raman spectra of Ge-I

5.4 Conclusions

It has been possible synthesize germanane by room temperature acid treatments. The reactions of CaGe2 with HCl and H_3PO_4 seem to be more favourable. Chemical modification of germanane by substitution of the Ge-H might help us in using germanane for various applications in near future.

REFERENCES

1. Dávila, M. E., *New J. Phys.* **2014,** 16.
2. Acun, A., *J. Phys.: Condens. Matter* **2015,** 27.
3. Zeyuan Ni, E. M., Yasunobu Ando, and Satoshi Watanabe, *Phys. Rev. B* **2017,** 96.
4. Bianco, E., *ACS Nano* **2013,** 7.
5. B N Madhushankar, A. K., T Giousis, G Potsi, D Gournis, P Rudolf, G R Blake,C H van der Wal and B J van Wees *2D Mater.* **2017,** 4.
6. Liu, Z., *Chem. Commun.* **2014,** 50.
7. Shishi Jiang, S. B., Elisabeth Bianco, Oscar D. Restrepo, Wolfgang Windl & Joshua E. Goldberger, *Nat. Comm.* **2014,** 5.
8. Paul H. Tobash, S. B., *J. Solid State Chem.* **2007,** 180.